Controlling factors of acoustic properties in continental carbonates: Implications for high-resolution seismic imaging

Cédric Bailly, T. Kernif, Y. Hamon, M. Adelinet, Jerome Fortin

Journal Pre-proof

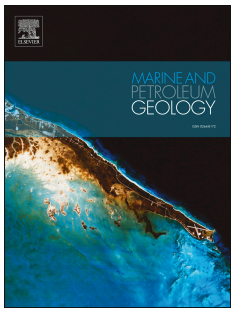

Controlling factors of acoustic properties in continental carbonates: Implications for high-resolution seismic imaging

C. Bailly, T. Kernif, Y. Hamon, M. Adelinet, J. Fortin

PII: S0264-8172(21)00621-8

DOI: https://doi.org/10.1016/j.marpetgeo.2021.105518

Reference: JMPG 105518

To appear in: *Marine and Petroleum Geology*

Received Date: 8 June 2021

Revised Date: 28 December 2021

Accepted Date: 29 December 2021

Please cite this article as: Bailly, C., Kernif, T., Hamon, Y., Adelinet, M., Fortin, J., Controlling factors of acoustic properties in continental carbonates: Implications for high-resolution seismic imaging, *Marine and Petroleum Geology* (2022), doi: https://doi.org/10.1016/j.marpetgeo.2021.105518.

Controlling factors of acoustic properties in continental carbonates: Implications for high-resolution seismic imaging

C. Bailly[1], T. Kernif[2], Y. Hamon[3], M. Adelinet[3] and J. Fortin[4]

[1]Université Paris-Saclay, CNRS, GEOPS, 91045, Orsay, France

[2]Univ Rennes, CNRS, Géosciences Rennes, UMR 6118, 35000 Rennes, France

[3]IFP Energies nouvelles, Geosciences Division, 1 et 4 Avenue de Bois-Préau, 92852 Rueil-Malmaison Cedex, France

[4]Laboratoire de Géologie, Ecole normale supérieure/CNRS UMR 8538, PSL Research University, 75005 Paris, France

Corresponding author: Cédric Bailly (cedric.bailly@universite-paris-saclay.fr)

Graphical abstract

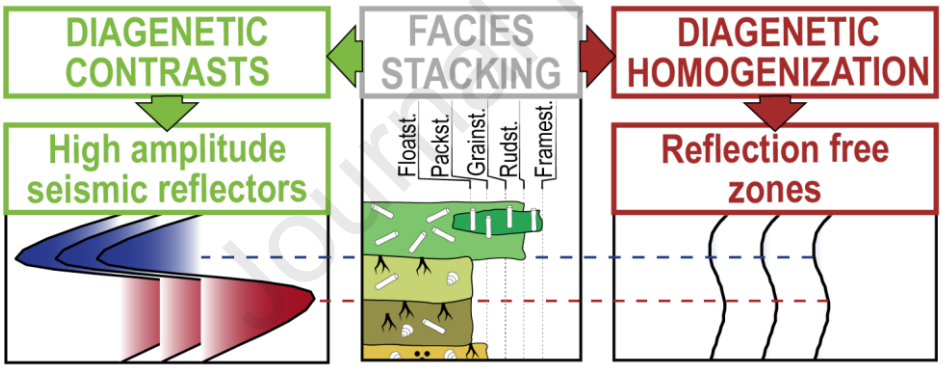

Highlights

- Investigation of palustrine and paludal tufa carbonates
- Facies and diagenetic characterizations of heterogeneous porous carbonates
- Multi-scale measurements of P-wave velocity in the laboratory and on outcrop
- Geological significance of synthetic seismograms equivalent to crosswell seismic
- Seismic imaging of continental carbonates is strongly controlled by diagenesis

Abstract

Continental carbonates are characterized by multi-scale heterogeneous porous networks, making the geological interpretation of seismic imaging difficult. We investigate two sedimentary sections exhibiting a similar facies succession, combining geological characterizations and multi-scale acoustic measurements. Based on outcrop investigation and petrographic description, we define nine sedimentary facies displaying contrasted early diagenetic evolutions. According to the vertical facies variations, we develop a depositional model corresponding to a low gradient valley fed by freshwaters, subdivided into three main domains (alluvial plain, palustrine and paludal). To understand the acoustic properties of the studied sedimentary rocks while remaining representative of their multi-scale heterogeneity, we acquire acoustic measurements at two different scales: i) at log-scale, directly on the outcrop surfaces using a frequency of 250 kHz; and ii) at plug-scale as usually done in laboratory using a frequency of 500 kHz. Based on these multi-scale geophysical acquisitions, we link *in-situ* P-wave velocities with the different sedimentary facies while characterizing centimeter-scale Representative Elementary Volumes (REVs). Conversely, based on laboratory measurements and thin-section petrography, we define relationships between P-wave velocity, porosity, facies, and diagenesis, corresponding to millimeter-scale REVs. Using both *in-situ* P-wave velocity measurements and plug densities, we construct 1-D synthetic seismograms showing meter-scale seismic reflectors equivalent to crosswell seismic frequency ranges. This approach shows the following: i) high-amplitude seismic reflectors fit with facies changes associated to diagenetic contrasts (*e.g.* cemented *versus* uncemented carbonates); ii) reflection free-zones match with a succession of facies changes affected by an extensive diagenetic homogenization (*e.g.* intensely to pervasively recrystallized and cemented carbonates). Our work highlights the importance of relating an extensive geological description of carbonates (facies, depositional model, diagenesis) together with multi-scale acoustic measurements and synthetic seismic modeling to predict the high-resolution heterogeneities of subsurface reservoirs.

Keywords

Continental carbonates, Paludal tufa, Palustrine environment, Diagenesis, Multi-scale porosity, Acoustic properties, Synthetic seismic, Seismic interpretation

1. Introduction

Seismic stratigraphy (sensu Vail et al., 1977), originally developed for marine, siliciclastic sediments and later applied to carbonate ones, is based on mapping of seismic reflectors that correspond to contrasts of acoustic impedances (Sheriff, 1977), thus geological contrasts having sedimentological and/or diagenetic origin (i.e., Fournier and Borgomano, 2007, Teillet et al., 2020, Zampetti et al., 2005). In order to understand the stratigraphic value of seismic reflectors, several studies modelled 2D synthetic seismic sections, based on seismic-size well-exposed outcrop descriptions together with punctual ultrasonic measurements of samples (e.g., Anselmetti et al., 1997a; Jafarian et al., 2018; Janson et al., 2007; Kenter et al., 2001; Kleipool et al., 2015, 2017; Stafleu et al., 1994; Stafleu and Sonnenfeld, 1994; Zeller et al., 2015). Assuming that plug-scale measurements are representative of decameter rock units, this approach is suitable for assessing the geological significance of reflectors representing large-scale geological heterogeneities within seismic resolution (size higher than 10 meters). Nevertheless, it is not accurate enough for discussing meter-scale heterogeneities, beyond seismic resolution, that are of crucial importance for the characterization of heterogeneous reservoirs. Fortunately, in order to better understand "sub-seismic" heterogeneities (*i.e.* meter-scale heterogeneities), crosswell seismic has been developed. Such method aims to image inter-well areas using high frequency acquisitions (between 100 and 2000 Hz), resulting in the imaging of reflectors representing meter-scale geological contrasts which bridge the gap between sonic log measurements and conventional seismic (e.g. Harris et al., 1995; Leiceaga et al., 2015; Yu et al., 2008). For instance, Parra et al. (2003) used a combination of nuclear magnetic resonance, sonic and density well logs with inverted impedance section based on crosswell seismic for characterizing the geometry of heterogeneous vuggy carbonates. Antonelli et al. (2004) demonstrated the benefit of crosswell seismic for detecting sub-seismic heterogeneities in order to adapt their development strategy in regard to the lateral variation of the reservoir compartmentalization. More recently, Beavington-Penney et al. (2019) imaged the lateral continuity of fourth-order cycles within a carbonate reservoir using crosswell seismic to better understand the architecture of flow units. However, if we want to accurately interpret crosswell seismic, we must understand the links between meter-scale geological heterogeneities and their seismic imaging. Indeed, these links can help to integrate petrophysical heterogeneities within reservoir model and thus accurately predict the

compartmentalization of carbonate reservoirs (Brigaud et al., 2014, Herlinger et al., 2017, Thomas et al., 2021, Vincent et al., 2020). To be consistent, such an approach must be applied on several geological objects highlighting different kinds of heterogeneities, including sedimentary facies, diagenesis and pore types.

Continental carbonates may develop in a broad range of sedimentary environments, including lacustrine and palustrine, hydrothermal, paludal, fluvial and alluvial settings (Alonso-Zarza and Tanner, 2010a). Consequently, they present a wide variety of sedimentary facies that may be modified by early diagenetic processes (Alonso-Zarza and Tanner, 2010b; Armenteros, 2010; De Boever et al., 2017), thus creating complex porous networks embedded in mono- to polygenic mineralogical fabrics including carbonates and non-carbonates elements. This multi-scale geological heterogeneity should imply a large variability of their acoustic properties. However, only a few studies exist that document the elastic properties of these sedimentary rocks and compare them to an accurate geological description (Bailly et al., 2019a; Fournier et al., 2018; Garcia-del-Cura et al., 2012; Regnet et al., 2019a; Reijmer et al., 2021; Soete et al., 2015; Vasquez et al., 2019). In this context, we focus our study on palustrine and paludal tufa carbonates. Following the definition of Freytet (1984), "a palustrine carbonate must present primary lacustrine depositional criteria (*e.g.* biota, sedimentary structures) together with evidences of subsequent exposure features (*e.g.* root traces, desiccation, …)". Consequently, these carbonates may develop in a wide range of lake environments. More specifically, paludal tufa carbonates accumulate exclusively in cool freshwater environments (Pedley, 1990). They correspond to calcite sediments accumulated under low depositional rates and ambient temperatures, forming poorly bedded and highly porous rocks (Capezzuoli et al., 2014). While the imaging of tufa carbonates was undertaken by Pedley and Hill (2002) with ground penetrating radar, there is a paucity of studies focusing on their petroacoustic properties and seismic imaging.

In this article, we investigated two study sites showing successions of heterogeneous paludal tufa and palustrine carbonates of Pliocene age belonging to the same geological formation (Kokkarion fm. of Samos Island, Greece; Weidmann et al., 1984). Sedimentary descriptions made at outcrop, as well as petrographic and petrophysical characterization of samples in the laboratory enabled us to build a sedimentary model and to define a paragenetic sequence. One of the main peculiarities of these

deposits is the occurrence of cm-size moulds of macrophyte stems typical of paludal environment (Pedley, 1990), which raises the question of plug measurement representativity (Ehrenberg, 2007). To characterize acoustic properties of such rocks that may have a Representative Elementary Volume (REV *sensu* Bear, 1972) higher than the length of regular plugs, we used *in-situ* measurements of P-wave velocity at outcrops (e.g. Matonti et al., 2015). Based on these *in-situ* P-wave velocity and plug density measurements, we built seismic traces at a frequency equivalent to crosswell seismic. Such an approach coupling multi-scale acoustic measurements and geological descriptions finally aimed at discussing the geological controlling factors of the acoustic properties and seismic imaging of palustrine and paludal tufa carbonates.

2. Study framework

The two study sites are located on Samos, a Greek island in the eastern part of the Cyclades, in the Aegean-Anatolian area (Fig. 1a). Samos is characterized by different extensional regimes. Since the middle Eocene (~ 45 Ma), the Hellenic subduction induced a major back-arc extension which has led to the exhumation of metamorphic core complex (Jolivet et al., 2013). During the middle Miocene, a slab tearing episode below the western margin of Anatolia induced a retreat of the western part of the slab. This led to a greater extension westward, thus splitting Cyclades and Menderes Massif areas (Jolivet et al., 2013). According to Ring et al. (1999), this peculiar structural pattern generated a local ENE-WSW sinistral strike-slip faulting corridor, resulting in the formation of two pull-apart basins in Samos (Fig. 1a). In this study, we focused on the eastern basin, the Mytilini Basin which contains a more than one-thousand-meter-thick succession of Mio-Pliocene sedimentary rocks unconformably deposited on a metamorphic basement and distributed in five lithostratigraphic formations (Weidmann et al., 1984; Fig. 1a and b). The age of the sedimentary infill is well-known and is based on palynological study, mammal fauna description and radiochronological dating on volcanic rocks (Ioakim and Koufos, 2009; Koufos et al., 2011; Pe-Piper and Piper, 2007; Fig. 1b). Two sections were studied: the Marina and the Antenna sections, located 5 km apart (Fig. 1a). They cover the Kokkarion formation that succeeds to the siliciclastic facies of the Mytilini formation (Fig. 1a and b) and is capped by an erosional surface

(Weidmann et al., 1984). The Kokkarion Fm. is thus attributed to the Zanclean period. The Marina section consists of a well-exposed outcrop (Fig. 2a, b, c; 37°41'24.96"N, 26°56'55.98"E), composed of two carbonate intervals (Units 1 and 3), separated by a clay-dominated interval (Unit 2). The Antenna section is located on the topmost part of a hill, showing a succession of meter-scale layers of carbonates (Fig. 2d, e; 37°44'20.98"N, 26°56'45.39"E).

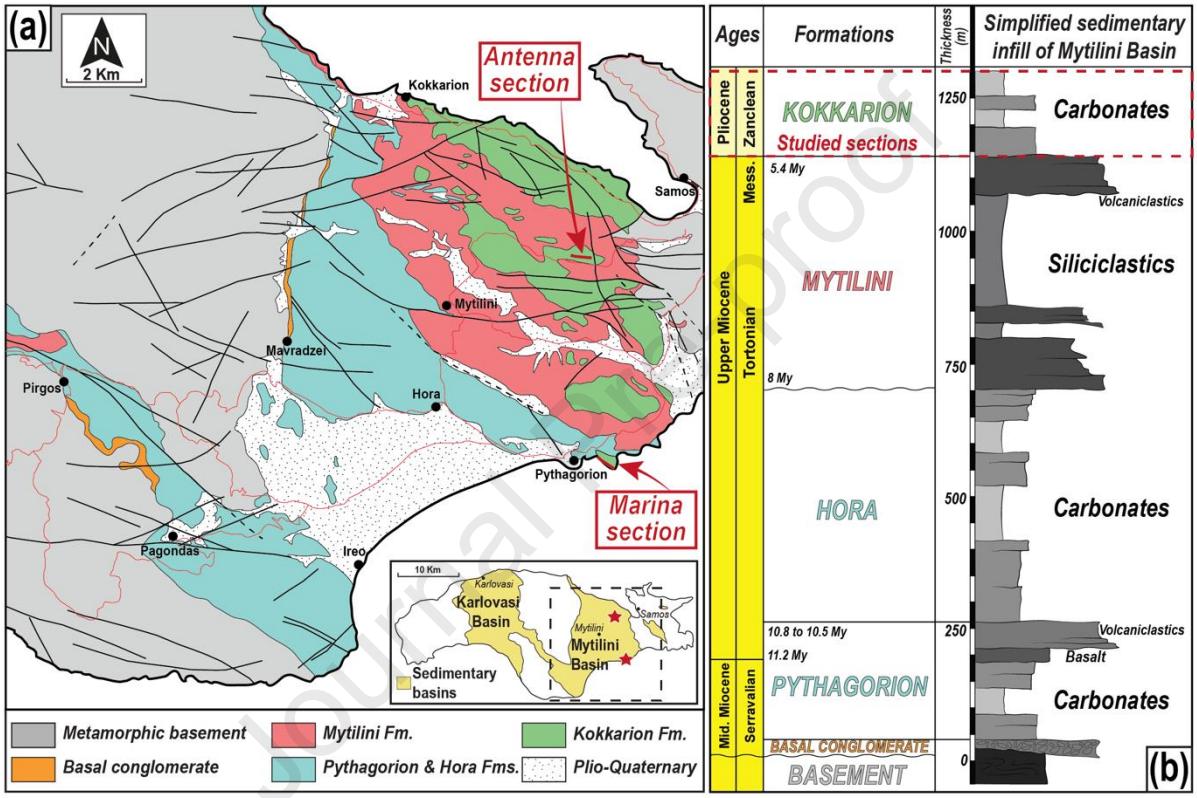

Fig. 1. Geological framework: (a) Map of Samos Island (Greece) showing the two sedimentary basins and the two study sites, with a focus on the Mytilini basin; (b) Stratigraphic column of the Mytilini basin (modified after Weidmann et al., 1984; Bailly et al., 2019a). Studied sections are part of the Kokkarion Formation.

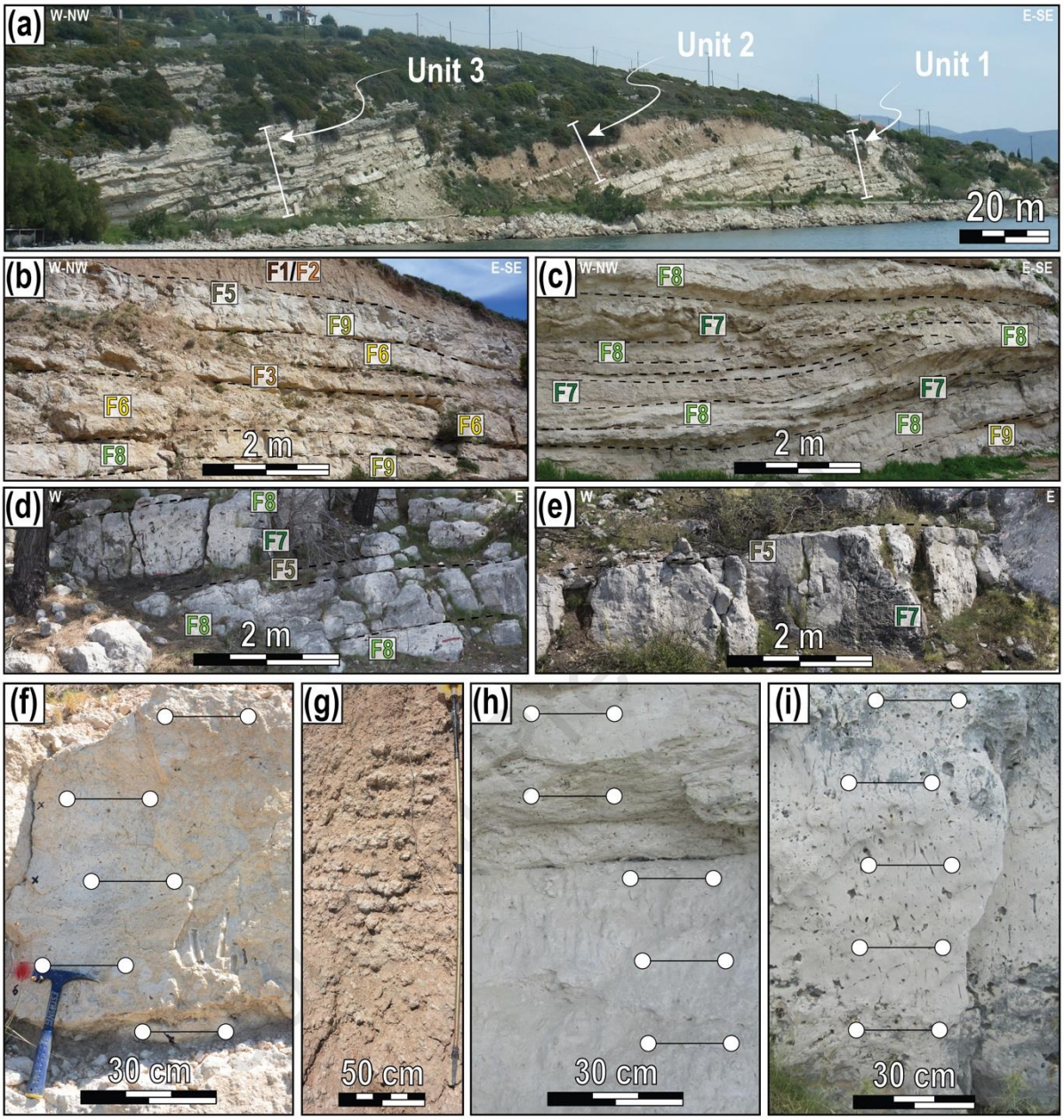

Fig. 2. Outcrop views and locations of *in-situ* acoustic measurements: (a) Panorama view of the Marina section highlighting three units; (b) Outcrop view of Unit 1, Marina section; (c) Outcrop view of Unit 3, Marina section; (d) Outcrop view of the Antenna section; (e) Outcrop view of the Antenna section; (f) Outcrop view of a single bed in the Marina section (Unit 1); (g) Outcrop view of clays and marls in the Marina section (Unit 2); (h) Outcrop view of two beds in the Marina section (Unit 3); (i) Outcrop view of a bed in the Antenna section. For (f), (h) and (i), the white circles and associated horizontal black lines correspond to the location of *in-situ* acoustic measurements.

3. Material and methods

3.1. Field work

3.1.1. Sedimentary geology and sampling

Geological field work (facies description, logging, …) was carried out on two sedimentary sections in June 2017 and June 2018 (Fig. 1a, Fig. 2). Considering the vertical facies variations, 57 samples were collected for laboratory characterization purposes (~ one sample per meter). No samples were collected in the Unit 2 of the Marina section, mainly due to the low cohesiveness of the outcropping rocks (Fig. 2a, g).

3.1.2. Acoustic measurements

A high-resolution *in-situ* acoustic characterization was performed using a portable acoustic device (Pundit PL-200, PROCEQ) with 250 kHz transducers for measuring P-wave velocities. The traveling times of P-waves (first break) were picked on the digital oscillograph's touchscreen and divided by the path length for obtaining the P-wave velocities. The acquisitions were done horizontally, parallel to the stratification, with a distance of 20 cm between the sensors. We used a gel (Sonctec 54-T04) to ensure a good coupling between the outcrop surfaces and the transducers. The uncertainty on the velocity measurements is dependent on the first break picking and on the path length measurements (error < 5 %). Note that the horizontal measurements did not take into account the occurrence of bedding planes (080/30N). These measurements were done with a constant vertical sampling rate – one measurement every 20 cm – which allowed us to characterize the P-wave velocity of meter-thick as well-as decimeter-thick beds using the same approach (Fig. 2f, h, i). Furthermore, the acoustic acquisitions were done on rock surfaces' that do not exhibit any evidence of large cracks and fractures. Therefore, the obtained results mainly reflect the properties of sedimentary rocks. Nevertheless, the impact of small scale structural heterogeneities can't be totally ruled out if the *in-situ* P-wave velocities variations are not comparable to the acoustic measurements performed in the lab (Matonti et al., 2015; Bailly et al., 2019b). Note that fewer *in-situ* measurements were carried out on the Unit 2 of the Marina section (Fig. 2a) due to the weak rock cohesiveness (lack of signal on the oscillograph).

Using *in-situ* P-wave velocity measurements aims to investigate sampling lengths higher than conventional plugs while characterizing centimeter-scale REV. Indeed, assuming a P-wave velocity in the range of 3000 $m.s^{-1}$ and 6000 $m.s^{-1}$, the used frequency (250 kHz) implies the generation of wavelength sizes in the range of 1.2 and 2.4 cm (upper bound of the characterized REV). Conversely, by analogy with seismic, the lower bound of the REV is higher than the quarter wavelength size, a value in the range of 0.3 and 0.6 cm for *in-situ* P-wave velocity measurements (Al-Chalabi, 2014; Sheriff and Geldart, 1995).

3.2. Laboratory analyses

3.2.1. Petrographic characterization

Fifty-seven thin sections were prepared, impregnated with blue epoxy to identify pore space. They were studied using both conventional and cathodoluminescence microscopy (CL). We used the Dunham (1962) and Choquette and Pray (1970) classifications for describing the limestone textures and the pore space. The main diagenetic phases were identified and organized chronologically according to their relative timing, mainly deduced from crosscutting relationships, as well as replacement and pseudomorphosis features. A visual quantification of the main diagenetic features was done (relative intensity from (0) *absent* to (5) *pervasive*). Additional SEM observations were performed for imaging the morphology of micrite and the microporous network of a few samples. We used the classification of Deville de Periere et al. (2011) for SEM observations.

3.2.2. Physical measurements

Depending on the sample size, horizontal plugs were cored with a diameter of 1 inch (25 mm) for 8 samples and 1.5 inch (40 mm) for 49 samples. The porosity and density were measured with the triple-weight method by assessing the plug mass under three different conditions: dried, fluid-saturated and fluid-saturated suspended in the saturating fluid. To ensure accurate measurements, we carefully followed this procedure:

- First, samples were dried in an oven during 48 hours at 60°C before measuring the dry-masses.

- Then, during a minimum timing of 24 hours, the dried-samples were placed in a desiccator connected to a vane pump to ensure the vacuum of the whole connected porosity (~ 10 Pa).

- A subsequent transfer of degassed and demineralised water within the desiccator was progressively done in order to ensure a fully saturation of the samples' connected porosity.

- Finally, saturated and apparent mass measurements were carried out and we calculated porosity and density.

P-wave velocities were obtained on dry samples using 500 kHz transducers connected to a manually controlled ultrasonic pulser-receiver system (5072PR, Olympus) and a digital oscilloscope (DPO4034B, Tektronix). A gel (Sonctec 54-T04) was used to ensure a good coupling between the plug surfaces and the transducers. The first breaks were directly measured on an oscillograph and divided by the length of the sample to compute the P-wave velocity. A constant and very low axial pressure was applied on the samples using a clamping device (120 kPa for the 1 inch plugs and 40 kPa for the 1.5 inch plugs). Given that we wanted to compare the laboratory measurements with the *in-situ* P-wave measurements, we did not realize those measurements under confining pressure. The uncertainty of the velocity measurements was mainly dependent on the first break picking (error < 5 %). Assuming a P-wave velocity in the range of 3000 and 6000 $m.s^{-1}$, the transducer frequency (500 kHz) implies the generation of wavelength sizes in the range of 6 mm and 1.2 cm, equal to the upper limit of the REV. Conversely, the lower limit of the REV is in the range of 1.5 mm and 3 mm (quarter wavelength criterion; Sheriff and Geldart, 1995, Al-Chalabi, 2014).

3.2.3. Statistical analyses

Statistical analysis was conducted, consisting of: 1) normal law computation to compare the P-wave velocities acquired both *in-situ* and in the laboratory; 2) violin plots computation (combination of a boxplot and a probability density) to look at the *in-situ* P-wave velocities in the light of facies classification; and 3) Kernel regression computation to highlight the vertical trends of the *in situ* P-wave velocity (smooth curves with a 95 per cent confidence interval). We used the package ggplot2 of R, a free software environment for statistical computing and graphics.

3.2.4. Synthetic seismic modelling

Based on the *in-situ* P-wave velocities and plug density measurements, synthetic seismic analyses were performed using EasyTrace™ Software (see Jafarian et al. (2018) for the equations). We computed the acoustic impedance, the reflectivity coefficient (RC) and finally the 1D seismic trace (zero offset) using a convolution on the RC with an analytical Ricker wavelet. We chose a central frequency of 500 Hz based on resolutions calculation. Indeed, for a P-wave velocity in the range of 3000-6000 $m.s^{-1}$, this central frequency implied a limit of resolvability of 1.5-3 meters (quarter wavelength criterion, Sheriff and Geldart, 1995; Al-Chalabi, 2014). This leads to characterize meter-scale impedance contrasts, comparable to the crosswell seismic resolution (approximately 3 meters according to Harris et al., 1995). For Marina section, because of the absence of density measurements for unit 2, acoustic impedance was computed assuming a linear extrapolation of density between 15 and 29 meters.

4. Results

4.1. Facies definition

4.1.1. F1: Reddish to brownish clays

Facies F1 consists of centimeter to meter-scale levels of monotonous reddish to brownish clays (Fig. 2a, g, Fig. 3a). The thickest layers may contain a few floating sub-rounded cm-size quartz clasts. Locally, isolated, nodular, whitish cm-size concretions are also observed and may be associated with root traces. This facies is only observed in the Marina section (Fig. 7a).

4.1.2. F2: Nodular and marly mudstone

Facies F2 corresponds to centimeter to decimeter layers of nodular and marly mudstone embedded in the reddish to brownish clays (Fig. 3b). It is not well-lithified, contains numerous root traces, cracks and rare sub-rounded to angular mm-size quartz clasts. F2 is only observed in the unit 2 of the Marina section, in association with F1 (Fig. 7a).

4.1.3. F3: Silty pedogenic mudstone/wackestone

263 At outcrop, the silty pedogenic mudstone/wackestone facies (F3) displays decimetre-scale beds
264 with irregular surfaces (Fig. 2b). It corresponds to light beige limestones containing a few bioclasts
265 (ostracods, gastropods), leaves and millimetric angular to sub-angular quartz (Fig. 3c) embedded in a
266 microporous micrite (Fig. 3d). Macro- or microscopically, F3 shows numerous root moulds that point
267 to a high pedogenic activity (Fig. 3c). This observation is strengthened by the occurrence of both curved
268 cracks and calcified root cells (Fig. 3d). The silty pedogenic mudstone and wackestone are only observed
269 in units 1 and 2 of the Marina section (Fig. 7a).
270
271 *4.1.4. F4: Quartz-rich floatstone*
272 Facies F4 corresponds to decimetre-thick beds showing an irregular base that may be of erosive
273 origin. It contains sub-rounded to sub-angular, mm-scale quartz grains embedded in a light beige matrix.
274 Microscopically, F4 shows numerous infra-millimetric angular to sub-angular quartz within a
275 microporous micrite (Fig. 3e). It displays locally a few carbonate clasts of millimeter size, mostly
276 phytoclasts (Fig. 3e). The quartz-rich floatstone shows only two occurrences in the unit 1 of the Marina
277 section (Fig. 7a).
278
279 *4.1.5. F5: Peloidal and intraclastic floatstone/wackestone*
280 This facies presents pluri-decimeter- to meter-thick tight beds often associated with exposure
281 surfaces at their tops (Fig. 2b, d, e). Macroscopically, the peloidal and intraclastic floatstone/wackestone
282 (Alonso-Zarza, 2003) presents a greyish matrix containing abundant root moulds. It displays also
283 pseudomicrokarsts (*sensu* Freytet and Verrechia, 2002; see part 4.2.4. for explanations) infilled with
284 millimeter rounded intraclasts embedded in a beige matrix. Microscopically, infra-millimeter rounded
285 peloids are widely observed, commonly surrounded by a calcitic cement (Fig. 3f). Numerous root casts
286 are also present (cemented root moulds *sensu* Klappa, 1980, Fig. 3f). Facies F5 is observed in both
287 studied sections (Fig. 7).
288
289 *4.1.6. F6: Bioclastic packstone/wackestone*

Facies F6 corresponds to thick massive beds showing irregular bases and tops, related to exposure surfaces (Fig. 2b). Macroscopic view of the bioclastic packstones and wackestones shows a beige to greyish matrix with root structures (Fig. 3g). In thin section, peloids, ostracods and gastropods and non-recognizable clasts are observed (Fig. 3h). Locally, some charophyte oogones are present, as well as phytoclasts, oncoids and rare silt-sized quartz. All these different elements are embedded in a dark micritic matrix. The bioclastic packstone and wackestone are mainly observed in the units 1 and 3 of the Marina section, but also at the topmost part of the Antenna section (Fig. 7).

4.1.7. F7: Phytoherm framestone

At outcrop, the phytoherm framestone occurs as decimetre to meter-thick patches and beds with irregular boundaries (Fig. 2c, d, e, Fig. 4a). They show millimeter to centimeter stem-moulds acting as a framework of anchored macrophytes in life position (Fig. 4b). Facies F7 is spatially closely related with facies F8 (Fig. 2c, Fig. 4a). Macroscopically, facies F7 displays dark beige calcite fringes mimicking macrophyte stems, surrounded by a light beige matrix (Fig. 4c). Microscopically, these fringes consist of polycyclic calcite sheets (Fig. 4d). Millimeter-size macropores embedded in a microsparitic to sparitic framework were also observed (Fig. 4e). They are partially to completely cemented and/or filled by a micritic to peloidal matrix. A few levels present frameworks of charophyte thalli. Facies F7 does not contain any detrital fraction. The phytoherm framestones are observed in both studied sections (Fig. 7).

4.1.8. F8: Phytoclastic rudstone

Facies F8 shows pluri-decimeter to meter-thick beds with irregular stratification, locally erosive base and exposure features (Fig. 2c, d). Macroscopically, the phytoclastic rudstones present dark beige millimeter to pluri-centimeter clasts of macrophyte stem relics embedded in a beige matrix with local macroporosity (Fig. 4f). The petrographic observations highlight preserved and broken microsparitic to sparitic phytoclasts surrounded by a dark micritic matrix (Fig. 4g). Gastropods, oncoids, charophyte thalli and oogones are also present. The macropores may be partly to totally filled by a calcitic cement.

A few beds of this facies contain a detrital fraction of silty quartz. The phytoclastic rudstone occurs in both studied sections (Fig. 7).

4.1.9. F9: Phytoclastic floatstone

The phytoclastic floatstone displays decimeter- to meter-thick massive beds associated with flat to irregular surfaces (Fig. 2b, c). Macroscopic observations show scattered dark beige oncoids and mm-sized phytoclasts embedded in a beige matrix (Fig. 4h). Microscopic observations show rounded micritic to microsparitic oncoids and phytoclasts surrounded by a dark micritic matrix, occasionally pervasively and highly microporous (Fig. 4i). The macropores may remained unfilled or partly to totally filled by calcitic cement. Few beds of F9 contain a detrital fraction of silty quartz. This facies is present in both studied sections (Fig. 7).

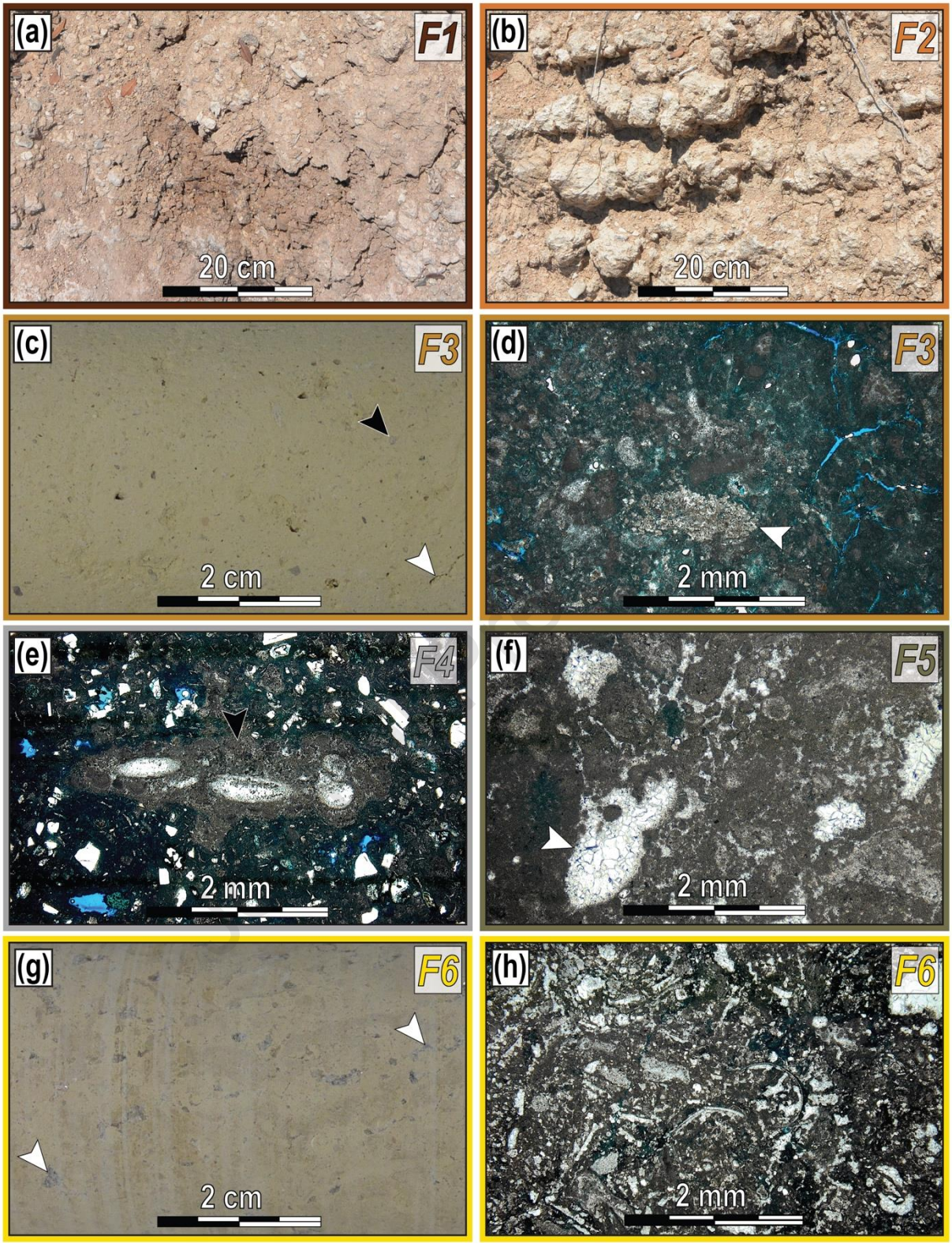

Fig. 3. Overview of the different facies (part 1). Color code used for each facies is the same throughout the manuscript. (a) F1: Macroscopic view, reddish to brownish clays (*unsampled*); (b) F2: Macroscopic view, nodular and marly mudstone (*unsampled*); (c) F3: Macroscopic view, silty pedogenic mudstone with root moulds (white arrow) and millimetric quartz (black arrow) ; (d) F3: PPL view, silty pedogenic mudstone with calcified root cells (white arrow) and microporous matrix (bluish brown colour of the matrix); (e) F4: PPL view, quartz-rich floatstone containing millimeter-size phytoclasts (black arrow); (f) F5 : PPL view, peloidal and intraclastic floatstone with root casts (white arrow); (g) F6: Macroscopic view, bioclastic packstone showing root casts (white arrows). (h) F6: PPL view, bioclastic packstone.

338

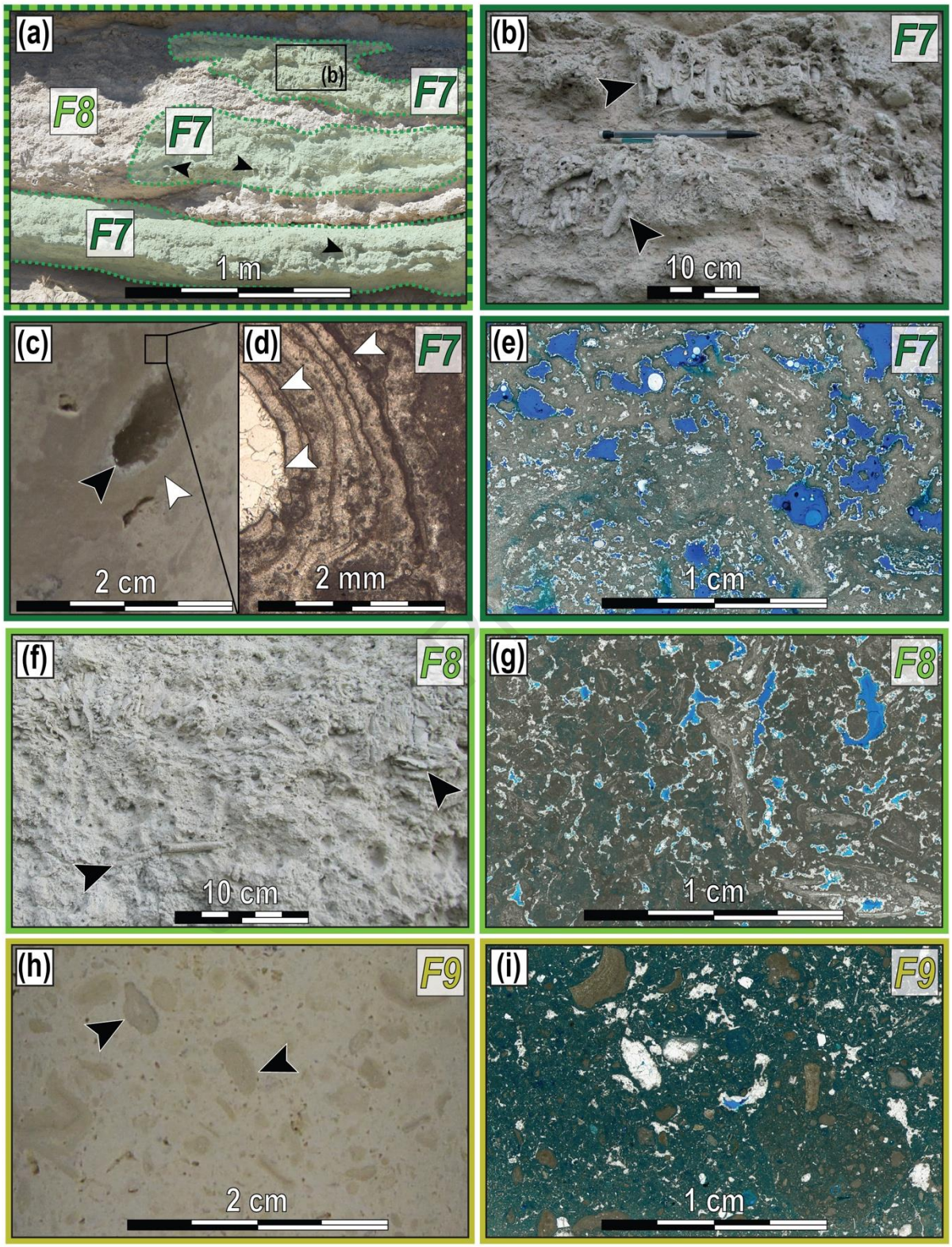

339
340 **Fig. 4.** Overview of the different facies (part 2). Color code used for each facies is the same throughout the
341 manuscript. (a) Outcrop view, phytoherm framestone beds and patches (F7) showing local centimeter-size moulds
342 of phragmite stems (black arrows), alternating with phytoclastic rudstones (F8); (b) F7: Macroscopic view,
343 phytoherm framestone with a framework of anchored macrophytes in life position (black arrows); (c) F7:
344 Macroscopic view, preserved stem-mould (black arrow) encrusted by a cement fringe (white arrow); (d) PPL view,
345 polycyclic cement fringes (white arrows); (e) F7: PPL view, phytoherm framestone showing a huge macroporous
346 framework (blue epoxy); (f) F8: Macroscopic view, phytoclastic rudstone composed of numerous reworked tufa
347 clasts (black arrows); (g) F8: Microscopic view, phytoclastic rudstone with a significant interparticular

macroporosity together with a microporous matrix (bluish brown colour of the matrix); (h) F9: Macroscopic view, phytoclastic floatstone including oncoids (black arrows); (i) F9: Microscopic view, phytoclastic floatstone with oncoids and reworked/broken phytoclasts embedded in a microporous matrix (bluish brown colour of the matrix).

4.2. Diagenetic characterization

All the facies described above show evidence of early diagenetic modifications. The various diagenetic phases, including multiple types of cement, dissolution and recrystallization events are described. They are organized chronologically, according to their relative abundance and timing (Fig. 5), mainly deduced from crosscutting relationships, observed in the field and during petrographic analyses. No microscopic characterization of facies F1 and F2 was done.

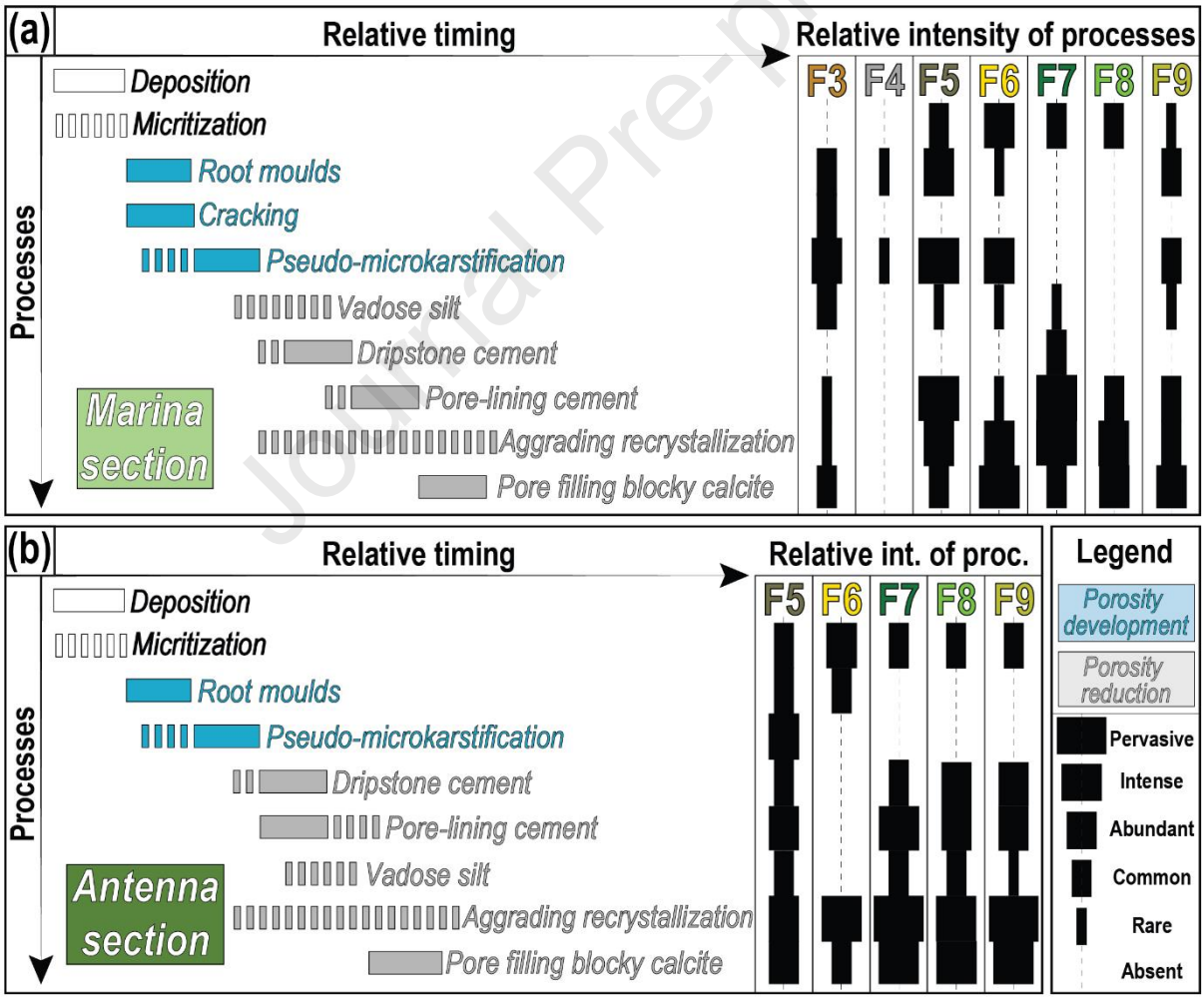

Fig. 5. Paragenetic sequences of the studied sections showing the relative intensity of each process sorted per facies: (a) Paragenesis for Marina section; (b) Paragenesis for Antenna Section. The legend explains the color code for porosity development or reduction and the relative intensity scale of the diagenetic processes.

4.2.1. Micritization

366 Micritization consists in the development of a micrite envelop around grains (gastropods,
367 charophyte thalli, ostracods). It also occurs at the surface of the polycyclic fringe sparitic cements
368 developed around the stem-moulds (Fig. 4d). Micritization is sporadically observed in facies F5, F6, F7,
369 F8 and F9 in the Marina and Antenna sections (Fig. 5).

370 Purser (1980) described such features in marine carbonates and associated them to a syn-
371 depositional process. Pedley (1992) also interpreted these "micrite fringes" as the earliest cements
372 developing around the macrophyte stems. Lettéron et al. (2017) observed micritized clasts in continental
373 carbonates located under subaerial surfaces. According to Swirydczuk et al. (1979), micro-boring by
374 endolithic algae around grains may be responsible of micritization.

375

376 *4.2.2. Root moulds*

377 Numerous root moulds are observed both at outcrop (vertical irregular tube-shaped root moulds,
378 Fig. 6a) and in hand samples (branched rootlet network, Fig. 6b). These moulds can be solution enlarged,
379 remained open or infilled by internal sediment, or various cements. They are commonly observed in
380 facies F2, F3, F5 and more rarely observed in facies F4, F6 and F9, in both studied sections (Fig. 5).

381 These root traces and moulds are classically associated to a pedogenic activity occurring in
382 palustrine setting (Freytet and Verrecchia, 2002).

383

384 *4.2.3. Cracking*

385 Circum-granular cracks are observed around oversized clasts (Fig. 6c). They are only identified
386 in facies F2 and F3 of the Marina section, in close association with root moulds (Fig. 5a).

387 These curved cracks (Freytet, 1984) outline desiccation episodes associated with the exposure
388 of sediments (Alonso-Zarza, 2003).

389

390 4.2.4. Microkarstification

391 Microkarstification is observed below irregular surfaces, with decimeter-size reliefs infilled by
392 a coarse brecciated material. Some of these structures still show enlarged root hollows, infilled by the
393 same breccia or by a calcite cement. Microscopically, a complex irregular network of "vuggy" porosity

394 is observed and infilled by vadose silt (geopetal structure) and granular to blocky calcite (Fig. 6d). These
395 "pseudomicrokarsts" (in the sense of Freytet and Verrecchia, 2002) are mainly observed in the Marina
396 section (Fig. 5a) and occur occasionally in the Antenna section (Fig. 5b). They are abundant to pervasive
397 in facies F5, common to abundant in facies F3 and F6 and F9, and rare in facies F4.

398 According to Freytet and Verrecchia (2002) "pseudomicrokarstification" is due to mechanical
399 enlargement of root traces and not dissolution. This feature is common in palustrine and lacustrine
400 environments and points to early diagenesis occurring in vadose environment.

401

402 *4.2.5. Vadose silt and dripstone cements*

403 Pseudomicrokarsts, root hollows, or other macropores may be partially affected by geopetal
404 infills composed of crystalline and vadose silts (Fig. 6d and f). Additionally, dripstone cements (*sensu*
405 Flügel, 2010, Fig. 6e and f) may also occur in the primary inter-framework voids of the phytoherm
406 framestone (F7) and in pseudomicrokarsts. The vadose silts are rarely to commonly observed in both
407 sections (Fig. 5). The dripstone cements are mainly observed within the Antenna section (Fig. 5b) in
408 facies F5, F7, F8 and F9. These cements are non-luminescent in CL. The timing of the vadose silt infill
409 with respect to other processes may vary between Marina and Antenna sections (Fig. 5). For the Marina
410 section, vadose silts occur before a subsequent pore-lining cement (Fig. 6d) while in the Antenna
411 section, they occur after pore-lining cement (Fig. 6f).

412 The pendant morphology generally indicates vadose conditions (Flügel, 2010), while the non-
413 luminescence suggests oxidizing conditions, also in line with a vadose environment (Meyers, 1991).
414 The specific distribution of these silts cements associated to roots and pseudomicrokarsts suggests an
415 early meteoric diagenesis in a vadose setting.

416

417 *4.2.6. Pore-lining cement fringe*

418 A pore-lining cement fringe may partially occlude the porosity of the studied carbonates. It
419 mostly consists of a granular calcite with crystal size comprised between 50 µm and 150 µm. Note that
420 one occurrence of early pore lining cement corresponds to an acicular cement (white arrow, Fig. 6f).
421 This phase succeeds dripstone cements (Fig. 6e) and occurs before or after vadose silt deposition

(Fig. 6d, f) It is mainly observed in facies F5 and F7, occasionally in facies F8 and F9, and more rarely in facies F3 and F6. The pore-lining cement is more common in the Antenna section than in the Marina section (Fig. 5a, b).

The cross-cutting relationships with dripstones and vadose silts indicate an early cement phase, probably associated to a meteoric phreatic setting.

4.2.7. Aggrading recrystallization

The subsequent diagenetic phase consists in aggrading recrystallization, implying an increase of the micrite crystal size. It occurs as patches within matrix (Fig. 6c) or affect intensely to pervasively the whole fabric of the studied carbonates (Fig. 6e, f, g). SEM observations within a recrystallized sample associated to root casts (Fig. 6g) show the presence of a serrate micrite with subrounded crystals surrounded by larger crystals with euhedral overgrowths (Fig. 6h). The intensity of this recrystallization process is higher in the Antenna section than in the Marina section. It is rare in facies F3 (Fig. 5a) and affects facies F5, F6, F7, F8 and F9 with different intensities (Fig. 5a, b).

Such a recrystallization process has already been described by Volery et al. (2010). These authors argued that these crystal morphologies are due to an LMC-LMC recrystallization within a phreatic lens, a hypothesis that can be advanced here, based on the crystal morphology and LMC mineralogy. Even if the timing of this phase is unclear, it seems coeval with the pore-lining and blocky cementation that occur early after deposition, in a meteoric phreatic setting.

4.2.8. Blocky calcite cement

Following the previous phases, a blocky calcite cementation occurs (Fig. 5). It consists of calcite crystals with sizes up to 500 µm (Fig. 6i). It totally fills the porosity (Fig.6 d, f, g, i). As highlighted by the CL pictures, different stages of calcite are identified (Fig. 6j). In most of the cases, it is non-luminescent with a few thin bright orange bands. Blocky calcite cement is mostly observed in the Antenna section, like the pore-lining cement and the recrystallization (Fig. 5b). It affects all the facies, except facies F4.

449 The crystal morphology and the luminescence pattern, similar to the older banded cement
450 (OBC) of Meyers (1991), suggest precipitation in an active freshwater phreatic zone (Dickson and
451 Saller, 1995).
452

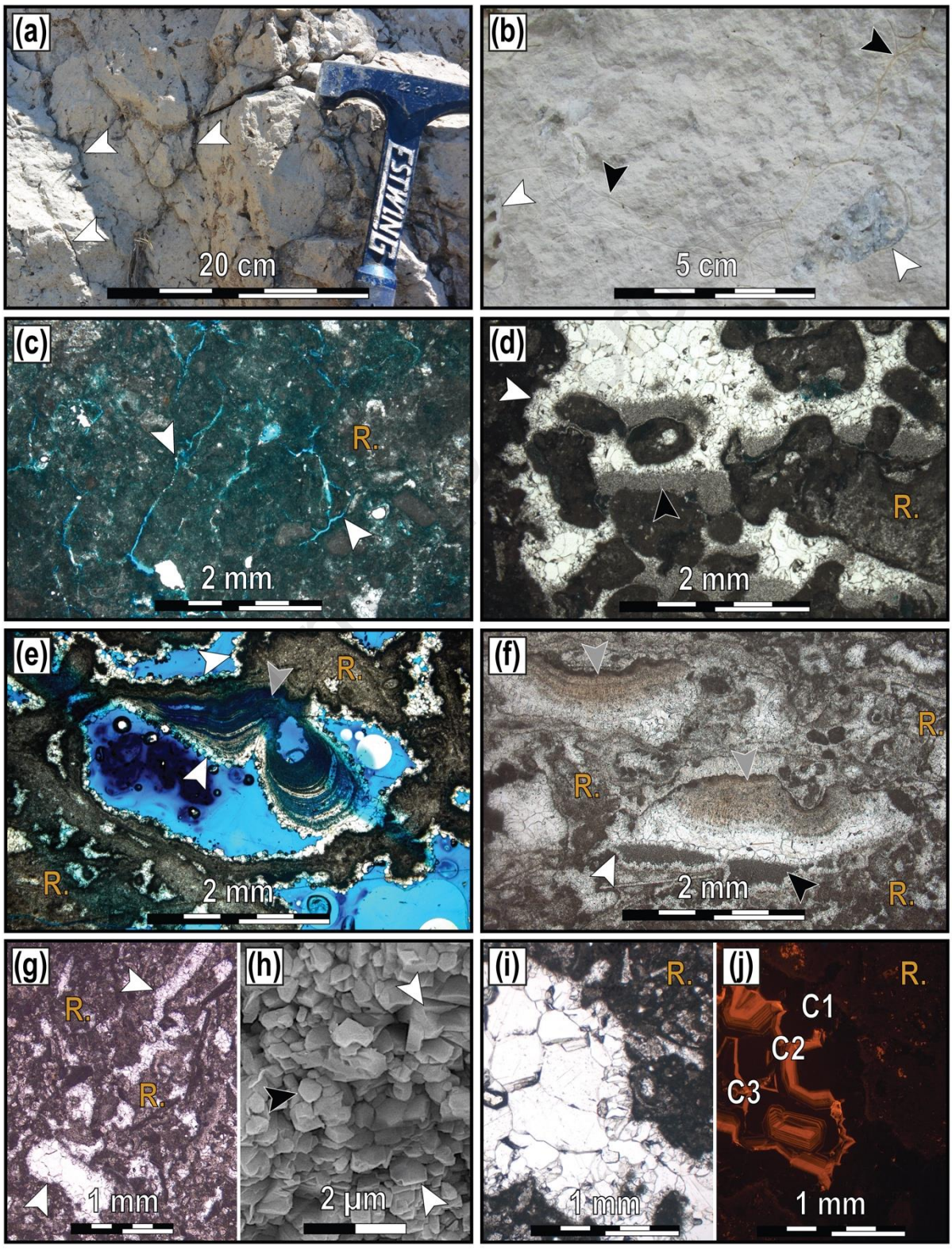

453
454 **Fig. 6.** Overview of the diagenetic processes: (a) Macroscopic view, root hollows (moulds; white arrows); (b)

Macroscopic view, root network (black arrows) and moulds of gastropods filled by a calcite cement (white arrows). (c) PPL view, open curved cracks. Note the recrystallized area (R); (d) PPL view, pseudomicrokarst cavity (white arrow) infilled by a vadose silt (black arrow) and a subsequent granular to blocky calcite. Note the recrystallized area (R); (e) PPL view, dripstone cement (grey arrow) and subsequent pore lining cement (white arrows). Note the recrystallized areas (R); (f) PPL view, pseudomicrokarst cavities infilled by a dripstone cement (grey arrows), pore lining cements (white arrow), vadose silt (black arrow) and a subsequent granular to blocky calcite. Note the important recrystallization of this sample (R); (g) PPL view, root casts (white arrows) and intense recrystallization (R) in a bioclastic packstone; (h) SEM view, serrate micrite showing subrounded crystals (black arrow) and euhedral overgrowths (white arrows); (i) and (j) PPL and corresponding CL views, multistage infill of a pseudomicrokarst showing three growth stages: C1 – Granular non-luminescent calcite, C2 – Drusy to blocky non-luminescent up to orange bright calcite; C3 – Non-luminescent blocky calcite with thin bright orange bands.

4.3. Description of the vertical evolution of facies and diagenesis

4.3.1. Marina section

The Marina section is divided in three main lithostratigraphic units (Fig. 7a). The first one consists of a 15 m thick succession of carbonate facies (F4, F5, F6, F7, F8 and F9) that alternate with reddish to brownish clays (F1) or silty pedogenic mudstone (F3). Whereas F1 and F3 are dominantly affected by root moulds and pseudomicrokarsts, carbonate beds show abundant recrystallization, and phreatic cement occluding the macroporosity. In a lesser extent, these carbonate beds also show root traces and erosive base. The topmost three meters of the unit 1 show the most intense diagenesis, with the highest occurrences of diagenetic phases.

The second unit, between 15 and 29.5 m, mainly consists of reddish to brownish clays (F1) showing occasional decimeter- to meter-scale beds of nodular and marly mudstone with numerous root traces (F2). A decimeter-thick tight bed of silty pedogenic mudstone (F3) capped by a 20 centimeter-thick bed of sandstone is also observed between 20 and 21 m.

The third unit (between 29.5 and 38 m) is dominated by pure carbonate rocks (F5, F6, F7 and F9). The base of the unit is highly affected by pedogenesis and shows numerous root traces and an upward increasing intensity of recrystallization and cementation. The second part of the unit is mainly dominated by decimeter- to meter-thick beds of heterogeneous tufa carbonates (F8 and F9). These beds show evidence of a common to intense recrystallization as well as a relatively rare cementation.

4.3.2. Antenna section

The Antenna section exclusively consists in pure carbonate facies F5, F6, F7, F8 and F9 (Fig. 7b). Between 0 m and 11.4 m, tufa-related facies occur (F7, F8, F9) showing intense to pervasive

recrystallization, with rare to common vadose features and a moderate to intense phreatic cementation. In these levels, numerous pedogenic exposure surfaces occur, associated with decimeter-thick beds of peloidal and intraclastic packstones. These beds show a common to intense recrystallization and phreatic cementation and some vadose features together with rarely preserved root moulds. The section is covered (not exposed) between 11,4 and 17 m.

Between 17 and 18.5 meters, several decimeter to meter-thick beds of tufa-related facies (F7, F8, F9) are observed, showing evidence of intense recrystallization and phreatic cementation. From 18.5 m to 20.8 m, meter-thick beds of peloidal and intraclastic packstone (F5) occur, dominated by root moulds, pseudomicrokarsts and phreatic cements. They are capped by decimeter-thick beds of recrystallized tufa-reworked facies (F8 and F9) up to 23 m. Finally, up to 24.5 m, bioclastic packstone (F6) occurs, showing numerous root traces at its top and an upward increasing recrystallization together with an abundant phreatic cementation.

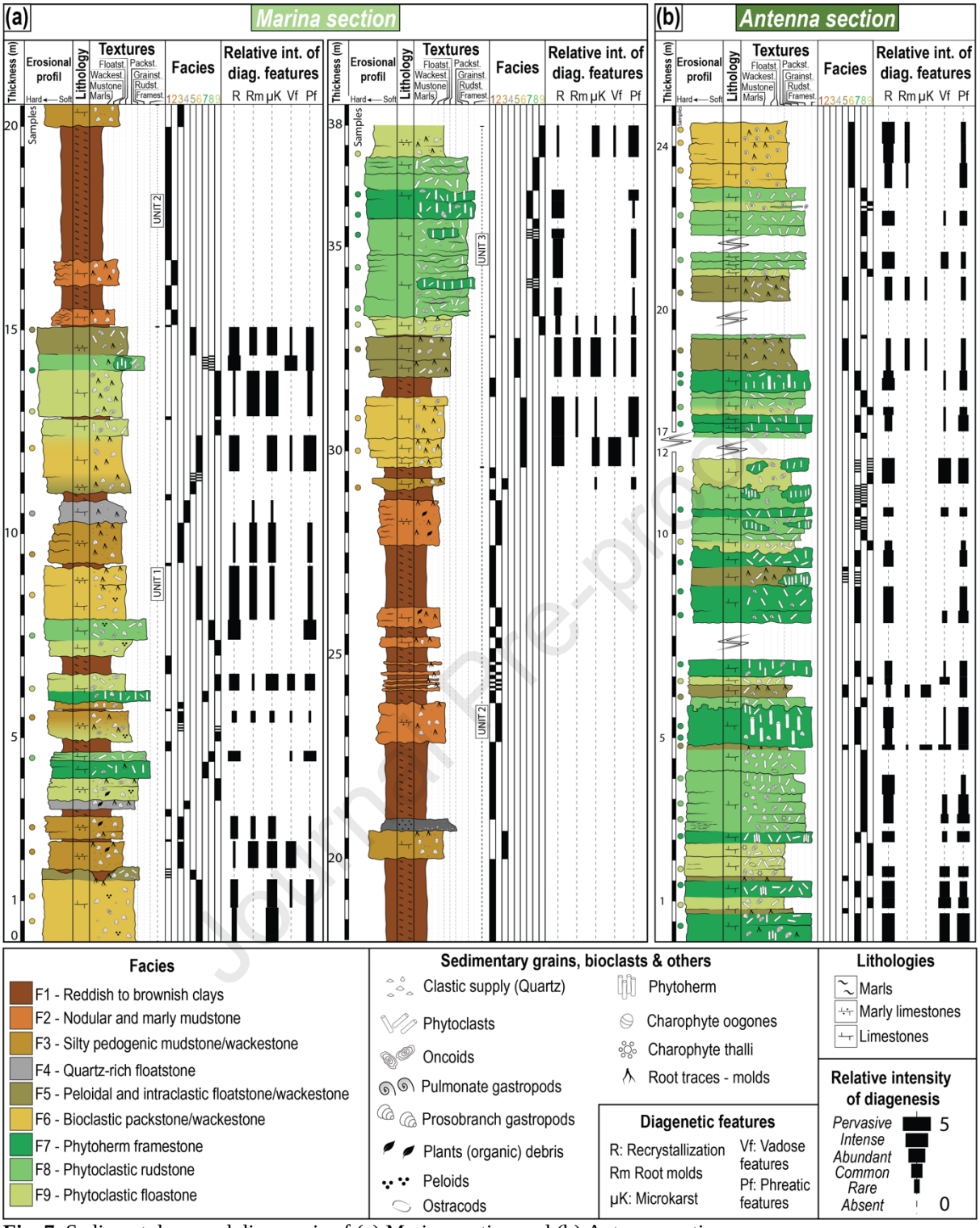

Fig. 7. Sedimentology and diagenesis of (a) Marina section and (b) Antenna section.

4.4. Multi-scale acoustic characterization

4.4.1. Laboratory dataset

The P-wave velocity-porosity data is compared to the empirical Raymer-Hunt-Gardner equation (RHG, Raymer et al., 1980) computed for a pure calcite medium in atmospheric conditions, indicating

a decrease of P-wave velocity with increasing porosity: $Vp_{RHG} = (1-\Phi)^2 * Vp_{Calcite} + \Phi * Vp_{Fluid}$ ($Vp_{Calcite}$ = 6400 m.s^{-1}; Vp_{Air} = 340 m.s^{-1}; Mavko et al., 2009). This equation assumes that the rocks are isotropic and monomineralic, well cemented and do not contain any crack-like or mould-like pores. Note that this equation is used to discriminate samples in the light of their pore geometries and mineralogical content. Here, we use the term "fitting with RHG" when our data are comprised within the +/- 5% of the RHG trend.

Table 1 summarizes the whole laboratory dataset, including petrographic characterization and petrophysical measurements. The statistical distribution of petrophysical properties are indicated in table 3. The Marina samples present scattered P-wave velocities (ranging between 2500 m.s^{-1} and 6200 m.s^{-1}; median = 5226 m.s^{-1}), associated with a large variation of porosity, from 3 % up to 29 % (Fig. 8a). A part of this dataset fits with RHG while a few samples exhibit higher (n =4) and lower (n = 8) P-wave velocity values than expected. The dataset exhibits normal law distributions for both P-wave velocity and porosity data (Fig. 8b and c). The Antenna samples shows high P-wave velocity values (from 5000 m.s^{-1} up to 6200 m.s^{-1}; median = 5880 m.s^{-1}) with porosity values lower than 8 % (Fig. 8a). Most of this dataset follows the RHG equation, except a few data that exhibit lower P-wave velocity than expected (P-wave velocity values lower than 5500 m.s^{-1}). Moreover, the dataset exhibits normal law distributions for both P-wave velocity and porosity data (Fig. 8b and c).

Fig. 9a, b presents the laboratory dataset sorted in the light of facies description. Concerning the Marina dataset (Fig. 9a), facies F3 presents porosity higher than 14 % and the lowest P-wave velocities of the dataset, even lower than the one expected by RHG (lowest values of the dataset). The only value available for the facies F4 is also lower than RHG. Facies F5 and F6 display values fitting with RHG, with porosity between 4 % and 16 % and P-wave velocity between 6000 m.s^{-1} and 4700 m.s^{-1}. Data corresponding to facies F7 shows porosity between 10 % and 22 % and P-wave velocity ranging between 6000 m.s^{-1} and 4500 m.s^{-1}, higher than expected with RHG. Facies F8 shows porosity between 3 % and 12 % and P-wave velocity ranging between 6200 m.s^{-1} and 5100 m.s^{-1} mostly fitting with RHG. Facies F9 displays porosity between 5 % and 17 % and P-wave velocity ranging between 5400 m.s^{-1} and 4100 m.s^{-1}, mostly lower than RHG except for one sample that is fitting with RHG. For the Antenna section (Fig. 9b), a few samples display lower P-wave velocity than expected with RHG (around 500

536 $m.s^{-1}$ and 1000 $m.s^{-1}$ lower), mainly corresponding to facies F5 and F7. Nevertheless, all other samples
537 are fitting with RHG prediction and no clear distinction can be made based on facies description.
538
539 *4.4.2. In-situ P-wave velocity dataset*
540 Table 2 summarizes the whole field dataset, including facies classification and *in-situ* acoustic
541 measurements. Statistical distribution of field dataset is also indicated in table 3. Fig. 8d shows the
542 unimodal distributions for the *in-situ* P-wave velocity measurements ($Vp_{in\text{-}situ}$) acquired on both sites.
543 The Marina *in-situ* P-wave velocities range between 800 $m.s^{-1}$ and 6300 $m.s^{-1}$ with a median of 3911 $m.s^{-1}$.
544 For the Antenna section, the $Vp_{in\text{-}situ}$ range between 2100 $m.s^{-1}$ and 6600 $m.s^{-1}$ with a median equal to
545 5618 $m.s^{-1}$. As for the plug P-wave velocities (Vp_{plug}), the $Vp_{in\text{-}situ}$ of the Antenna section are higher than
546 the ones measured in the Marina section (Fig. 8d). The $Vp_{in\text{-}situ}$ acquired on the Marina section present
547 a higher variability than the one measured on Antenna section.
548 We can describe the P-wave velocity signature according to the facies classification using violin
549 plots (Fig. 9c and d). For the Marina section (Fig. 9c), data obtained on facies F1 and F2 presents low
550 $Vp_{in\text{-}situ}$ values, lower than 1500 $m.s^{-1}$ for the reddish to brownish clays and mainly comprised between
551 2000 $m.s^{-1}$ and 3000 $m.s^{-1}$ for the nodular and marly mudstone. Most of facies F3 and F4 presents $Vp_{in\text{-}situ}$
552 lower than 3000 $m.s^{-1}$. Then, two groups of carbonate facies can be defined: i) a first group with high
553 $Vp_{in\text{-}situ}$ (higher than 4000 $m.s^{-1}$, low dispersion of data around the median) corresponding to facies F5
554 and F6; and ii) a second group with scattered $Vp_{in\text{-}situ}$ (from 2000 $m.s^{-1}$ up to 6000 $m.s^{-1}$, high dispersion
555 with flattened probability density) corresponding to facies F7, F8 and F9. Concerning the Antenna
556 dataset (Fig. 9d), most of the identified facies present high $Vp_{in\text{-}situ}$, ranging between 4000 $m.s^{-1}$ and
557 6500 $m.s^{-1}$ (facies F5, F7, F8 and F9), while facies F6 presents $Vp_{in\text{-}situ}$ lower than 4500 $m.s^{-1}$. For facies
558 F7, F8 and F9, a distinction should be done between the two sections. We observe a flattened probability
559 density associated with large interquartile values for the Marina section (Fig. 9c), while the probability
560 density mimics a normal distribution associated with lower interquartile values for the Antenna section
561 (Fig. 9d).
562

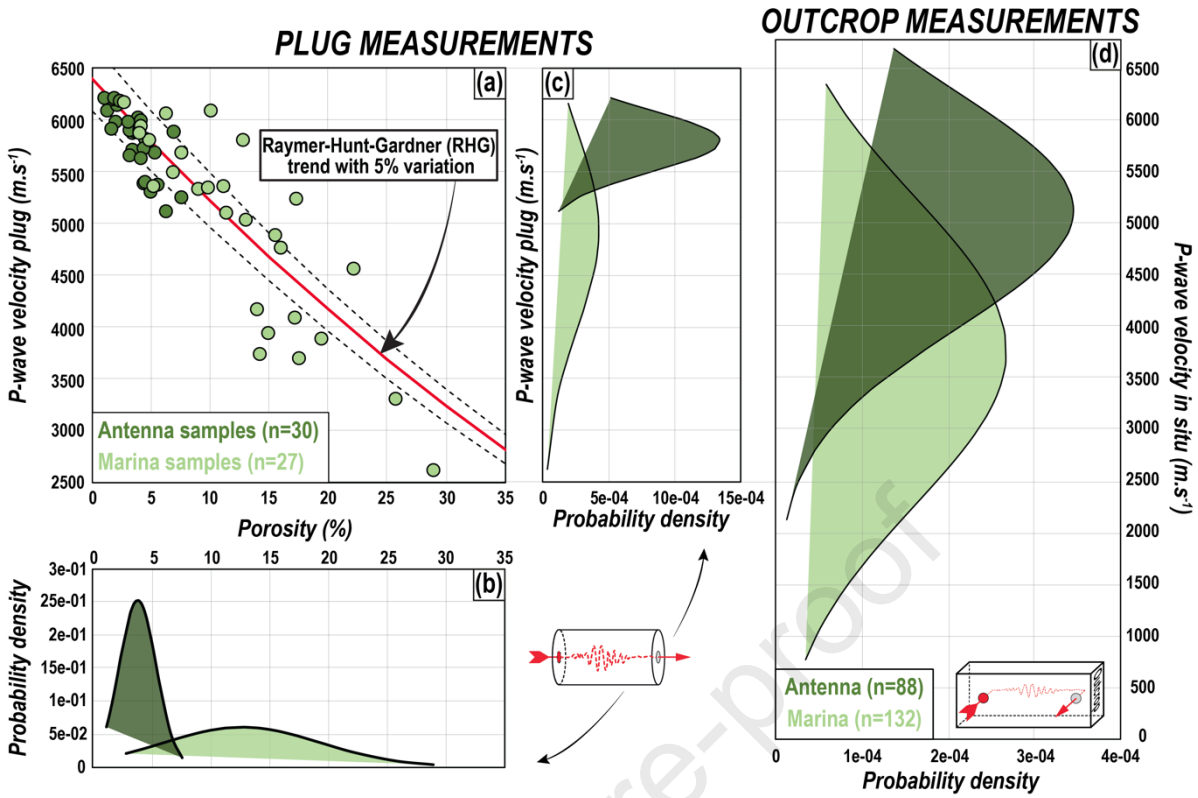

Fig. 8. Overview of the P-wave velocity and porosity datasets: (a) P-wave velocity acquired on plugs (500 kHz) *versus* porosity for Antenna and Marina samples. The Raymer-Hunt-Gardner trend is indicated with 5% variation; (b) and (c) Corresponding probability densities of porosity and P-wave velocity for Antenna and Marina samples; (d) Probability density of *in-situ* P-wave velocity for Antenna and Marina sections.

Table 1. Dataset of petrographic characterization and petrophysical measurements acquired on samples.

Section	Thickness (m)	Sample	Facies	Diagenetic typing	Vp ($m.s^{-1}$)	Phi (%)	Density (g.cm3)
Marina	0,6	MA01	F6	Recristallization + Cementation	5319	9,00	2,46
Marina	1,2	MA02	F6	Recristallization + Cementation	5488	6,88	2,51
Marina	2,2	MA03	F3	Root mold, no cement + Microphi	3697	17,58	2,21
Marina	2,8	MA04	F3	Root mold, no cement + Microphi	3929	14,99	2,29
Marina	4,6	MA05	F8	Recristallization + Cementation	6156	2,82	2,61
Marina	5,4	MA06	F3	Microcracks + Microporous matrix	3734	14,29	2,30
Marina	6,2	MA07	F9	Recristallization + Cementation	5348	5,29	2,56
Marina	7,4	MA08	F8	Recristallization + Cementation	5794	4,86	2,57
Marina	8,4	MA09	F6	Root mold, cement + Microphi mx.	4751	16,11	2,26
Marina	9,4	MA10	F3	Microcracks + Microporous matrix	2611	29,00	1,89
Marina	10,6	MA11	F4	Microporous matrix	3878	19,53	2,12
Marina	12,2	MA12	F6	Recristallization + Cementation	5677	7,62	2,50
Marina	13	MA13	F9	Root mold, cement + Microphi mx.	4873	15,60	2,29
Marina	14	MA14	F7	Heterogeneous macroporosity	5795	12,82	2,36
Marina	15	MA15	F5	Root mold, cement + Microphi mx.	5342	11,14	2,41
Marina	29,1	MA16	F3	Microporous matrix	3295	25,81	2,00
Marina	30,1	MA17	F6	Recristallization + Cementation	5923	4,17	2,60
Marina	30,9	MA18	F6	Recristallization + Cementation	5867	4,07	2,60
Marina	32,5	MA19	F5	Root mold, cement + Microphi mx.	5025	13,06	2,35
Marina	33,1	MA20	F9	Microcracks + Microporous matrix	4166	13,99	2,30
Marina	33,5	MA21a	F8	Heterogeneous macroporosity	5337	9,89	2,43
Marina	33,5	MA21b	F8	Heterogeneous macroporosity	5094	11,39	2,39
Marina	35,1	MA22	F8	Heterogeneous macroporosity	6056	6,37	2,49
Marina	35,3	MA24	F7	Heterogeneous macroporosity	4554	22,27	2,08
Marina	35,7	MA25	F7	Heterogeneous macroporosity	5226	17,37	2,22

Marina	36,3	MA26	F7	Heterogeneous macroporosity	6080	10,08	2,42
Marina	37,3	MA27	F9	Microporous matrix	4088	17,24	2,23
Antenna	0,4	AN 01	F7	Recristallization + Cementation	5900	3,67	2,59
Antenna	0,8	AN 02	F9	Recristallization + Cementation	5703	4,37	2,57
Antenna	1,4	AN 03	F7	Recristallization + Cementation	5659	3,88	2,56
Antenna	1,7	AN 04	F9	Recristallization + Cementation	6072	1,37	2,65
Antenna	2,6	AN 05	F7	Recristallization + Cementation	5969	2,03	2,63
Antenna	3	AN 06	F8	Recristallization + Cementation	6129	2,12	2,63
Antenna	3,4	AN 07	F8	Recristallization + Cementation	6180	1,82	2,63
Antenna	4	AN 08	F8	Recristallization + Cementation	6003	3,91	2,57
Antenna	4,8	AN 09	F5	Recristallization + Cementation	6201	1,15	2,64
Antenna	5	AN 10	F7	Recristallization + Cementation	5896	1,68	2,63
Antenna	5,3	AN 11	F7	Recristallization + Cementation	5694	3,51	2,43
Antenna	6	AN 12	F5	Microporous matrix	5110	6,38	2,51
Antenna	6,4	AN 13	F9	Recristallization + Cementation	5800	4,60	2,53
Antenna	6,8	AN 14	F7	Recristallization + Cementation	5373	4,46	2,55
Antenna	8	AN 15	F7	Recristallization + Cementation	5859	3,44	2,57
Antenna	8,6	AN 14‘	F7	Recristallization + Cementation	5640	3,21	2,49
Antenna	9,3	AN 17	F7	Recristallization + Cementation	6194	1,92	2,62
Antenna	9,8	AN 18	F9	Microporous matrix	5240	7,58	2,48
Antenna	10,6	AN 19	F7	Recristallization + Cementation	5880	3,68	2,59
Antenna	11,6	AN20	F9	Recristallization + Cementation	5978	4,16	2,59
Antenna	17,2	AN21	F7	Recristallization + Cementation	5393	4,53	2,58
Antenna	17,6	AN22	F8	Recristallization + Cementation	5619	4,23	2,58
Antenna	18,2	AN23	F7	Recristallization + Cementation	5893	4,09	2,59
Antenna	18,4	AN 24	F7	Heterogeneous macroporosity	5881	6,88	2,55
Antenna	19	AN 25	F5	Microporous matrix	5676	5,37	2,52
Antenna	20,4	AN 26	F5	Recristallization + Cementation	5298	5,03	2,54
Antenna	21,2	AN 27	F8	Recristallization + Cementation	5887	3,26	2,60
Antenna	22,3	AN 28	F8	Recristallization + Cementation	6169	2,43	2,61
Antenna	23,4	AN 29	F6	Recristallization + Cementation	5366	5,62	2,53
Antenna	24,1	AN 30	F6	Recristallization + Cementation	5715	4,46	2,56
Antenna	24,4	AN 31	F6	Recristallization + Cementation	5965	3,16	2,57

Table 2. Dataset of field characterization and *in situ* acoustic measurements.

Section	Thickness (m)	Facies	Vp (m.s^{-1})
Marina	0	F6	5181
Marina	0.2	F6	5348
Marina	0.4	F6	4831
Marina	0.6	F6	4831
Marina	0.8	F6	4963
Marina	1	F6	4396
Marina	1.2	F6	5405
Marina	1.4	F6	5571
Marina	1.6	F5	5362
Marina	1.8	F5	5405
Marina	2	F3	2333
Marina	2.2	F3	3231
Marina	2.4	F3	2133
Marina	2.6	F3	2676
Marina	2.8	F3	1818
Marina	3	F3	2532
Marina	3.2	F3	2139
Marina	3.4	F4	1963
Marina	3.6	F9	3976
Marina	3.8	F9	4320

Section	Thickness (m)	Facies	Vp (m.s^{-1})
Marina	32.9	F9	2005
Marina	33.1	F9	1550
Marina	33.3	F9	2712
Marina	33.5	F8	5195
Marina	33.7	F8	4640
Marina	33.9	F7	5666
Marina	34.1	F7	5666
Marina	34.3	F7	4444
Marina	34.5	F8	4863
Marina	34.7	F8	3279
Marina	34.9	F8	3257
Marina	35.1	F8	2469
Marina	35.3	F7	3106
Marina	35.5	F7	3431
Marina	35.7	F7	5115
Marina	36.1	F7	2326
Marina	36.3	F7	2397
Marina	36.5	F8	5291
Marina	36.7	F8	4515
Marina	36.9	F8	2778

Marina	4	F9	4292
Marina	4.2	F7	4950
Marina	4.4	F7	3333
Marina	4.6	F7	3415
Marina	4.8	F1	1485
Marina	5	F9	2857
Marina	5.2	F9	4444
Marina	5.4	F3	3145
Marina	5.6	F3	4415
Marina	5.8	F3	2257
Marina	6	F7	5464
Marina	6.2	F7	5464
Marina	6.4	F9	5587
Marina	6.6	F9	5747
Marina	6.8	F1	1172
Marina	7	F9	2286
Marina	7.2	F9	2954
Marina	7.4	F8	5864
Marina	7.6	F8	3571
Marina	7.8	F8	2387
Marina	8	F6	2778
Marina	8.2	F6	1786
Marina	8.4	F6	3442
Marina	8.6	F6	2581
Marina	8.8	F6	2293
Marina	9	F6	2425
Marina	9.2	F3	1916
Marina	9.4	F3	2233
Marina	9.6	F3	1972
Marina	9.8	F3	1954
Marina	10	F3	1754
Marina	10.2	F3	2230
Marina	10.6	F4	1798
Marina	10.8	F4	2653
Marina	11	F5	1864
Marina	11.2	F5	3935
Marina	11.4	F5	5249
Marina	11.6	F6	5013
Marina	11.8	F6	6079
Marina	12	F6	5775
Marina	12.2	F6	5775
Marina	12.4	F6	5607
Marina	12.6	F9	5296
Marina	12.8	F9	4167
Marina	13	F9	5751
Marina	13.2	F9	5263
Marina	13.4	F9	4902
Marina	13.6	F9	5530
Marina	13.8	F9	5075
Marina	14	F7	4545
Marina	14.2	F7	5333
Marina	14.4	F7	4751
Marina	14.6	F5	4267
Marina	14.8	F5	5075
Marina	37.1	F8	4396
Marina	37.3	F9	1980
Antenna	0	F7	6079
Antenna	0.2	F7	6689
Antenna	0.4	F7	5714
Antenna	0.6	F7	5714
Antenna	0.8	F5	6536
Antenna	1	F9	6349
Antenna	1.2	F7	5917
Antenna	1.4	F7	5634
Antenna	1.6	F5	6116
Antenna	1.8	F9	6116
Antenna	2	F9	6116
Antenna	2.2	F9	6116
Antenna	2.4	F9	5013
Antenna	2.6	F7	6116
Antenna	2.8	F8	5102
Antenna	3	F8	5038
Antenna	3.2	F8	5602
Antenna	3.4	F8	5420
Antenna	3.6	F8	5988
Antenna	3.8	F8	5291
Antenna	4	F8	6250
Antenna	4.2	F8	6079
Antenna	4.4	F8	4890
Antenna	4.6	F8	4577
Antenna	4.8	F5	5935
Antenna	5	F7	5780
Antenna	5.2	F7	6623
Antenna	5.4	F7	6250
Antenna	5.6	F7	5714
Antenna	5.8	F8	3448
Antenna	6	F5	4175
Antenna	6.2	F5	5277
Antenna	6.4	F9	3053
Antenna	6.6	F7	5814
Antenna	6.8	F7	4454
Antenna	7.8	F7	5063
Antenna	8	F7	5970
Antenna	8.2	F7	6472
Antenna	8.4	F7	4695
Antenna	8.6	F7	5731
Antenna	8.8	F7	5731
Antenna	9	F5	6079
Antenna	9.2	F5	6079
Antenna	9.4	F7	5181
Antenna	9.6	F9	5731
Antenna	9.8	F9	5731
Antenna	10	F8	5731
Antenna	10.2	F8	5917
Antenna	10.4	F8	6579
Antenna	10.6	F7	6545
Antenna	10.8	F8	5495
Antenna	11	F8	5731

Marina	15	F5	5128
Marina	15.2	F2	2532
Marina	15.4	F2	3909
Marina	16.2	F2	2317
Marina	16.4	F2	2083
Marina	16.6	F2	2128
Marina	20	F3	2947
Marina	20.2	F3	4282
Marina	20.4	F3	3913
Marina	20.6	F3	5000
Marina	23	F2	778
Marina	23.2	F2	1370
Marina	25.4	F2	2679
Marina	25.6	F2	2882
Marina	25.8	F2	3297
Marina	26	F2	1771
Marina	28.3	F2	2444
Marina	28.5	F2	2538
Marina	28.7	F1	1014
Marina	28.9	F1	1433
Marina	29.1	F3	2109
Marina	29.5	F3	2151
Marina	29.7	F6	3668
Marina	29.9	F6	5143
Marina	30.1	F6	6333
Marina	30.3	F6	5337
Marina	30.5	F6	5865
Marina	30.7	F6	5525
Marina	30.9	F6	5602
Marina	31.1	F6	5970
Marina	31.3	F6	5970
Marina	31.9	F5	5102
Marina	32.1	F5	4878
Marina	32.3	F5	5222
Marina	32.5	F5	4717
Marina	32.7	F5	2252

Antenna	11.2	F9	6711
Antenna	11.4	F9	6472
Antenna	11.6	F9	5917
Antenna	17	F7	3883
Antenna	17.2	F7	4202
Antenna	17.4	F9	2959
Antenna	17.6	F8	5764
Antenna	17.8	F8	6173
Antenna	18	F8	5666
Antenna	18.2	F7	2513
Antenna	18.4	F7	4988
Antenna	18.6	F5	5831
Antenna	18.8	F5	5128
Antenna	19	F5	5780
Antenna	19.2	F5	5780
Antenna	19.4	F8	4988
Antenna	20.2	F5	5263
Antenna	20.4	F5	4545
Antenna	20.6	F5	4444
Antenna	20.8	F9	4435
Antenna	21	F8	2817
Antenna	21.2	F8	3236
Antenna	21.4	F8	3328
Antenna	22	F8	4124
Antenna	22.2	F8	2353
Antenna	22.4	F8	5450
Antenna	22.6	F9	4556
Antenna	22.8	F8	2128
Antenna	23	F6	4367
Antenna	23.2	F6	4367
Antenna	23.4	F6	3067
Antenna	23.6	F6	3210
Antenna	23.8	F6	3929
Antenna	24	F6	3781
Antenna	24.2	F6	2793
Antenna	24.4	F6	3781

Table 3. Statistical distribution of petrophysical properties.

Statistical distribution	**Marina section**				**Antenna section**			
	Vp $_{plug}$	**Porosity**	**Density**	**Vp $_{in\ situ}$**	**Vp $_{plug}$**	**Porosity**	**Density**	**Vp $_{in\ situ}$**
Median	5226	13	2.36	3911	5880	4	2.57	5618
Mean	4930	13	2.35	3757	5785	4	2.57	5138
Std. dev.	954	7	0.19	1487	297	2	0.05	1153
Min	2611	3	1.89	778	5110	1	2.43	2128
Max	6156	29	2.61	6333	6201	8	2.65	6711

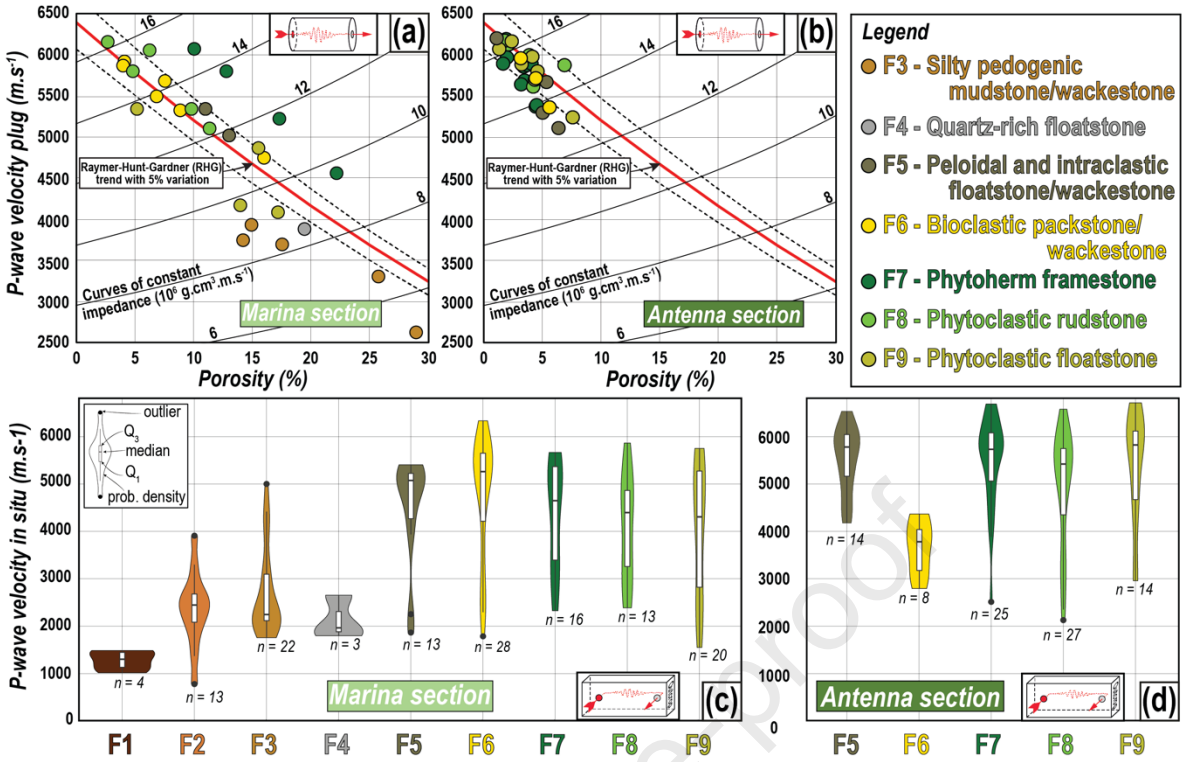

Fig. 9. Facies control of P-wave velocity: (a) P-wave velocity versus porosity at plug scale for Marina section and (b) Antenna section; (c) Violin plots of P-wave velocities acquired at outcrop scale for Marina section and (d) Antenna section.

4.5. Vertical evolution of the physical properties and associated high resolution seismic

4.5.1. Marina section

In Fig. 10, the geological descriptions of the Marina section are compared with physical properties acquired in laboratory and on outcrop, together with the resulting synthetic seismic trace. Generally, when the plug porosity increases, the *in-situ* P-wave velocity decreases, and *vice versa*. The plug (Vp_{plug}) and *in-situ* ($Vp_{in\text{-}situ}$) P-wave velocity measurements show the same vertical trends.

In the first unit, the vertical evolution of P-wave velocity shows a rough correlation with facies: detrital-rich facies (F1 to F4) are associated with relatively high to moderate porosity (15 to 30 %) and low P-wave velocity (1500 to 3000 $m.s^{-1}$), whereas pure carbonate facies (F5 to F9) rather show low to moderate porosity (3 to 15 %) and high P-wave velocity (4000 to 6000 $m.s^{-1}$). The first half of the unit (up to 8m) is therefore characterized by abrupt vertical changes of $Vp_{in\text{-}situ}$, and the second one by more homogeneous and blocky patterns.

Only few data are available for the second unit and mainly correspond to hard layers made of facies F2 and F3. They display relatively low $Vp_{in\text{-}situ}$, varying mainly between 1000 $m.s^{-1}$ and 3000 $m.s^{-}$

[1]. An unique level shows moderate to high values of $Vp_{in\text{-}situ}$ between 20 and 21 meters (between 3000 $m.s^{-1}$ and 5000 $m.s^{-1}$).

The third unit displays abrupt vertical changes of $Vp_{in\text{-}situ}$, but no obvious correlations with facies are observed. The first half of the unit (facies F6, F1 and F5) is characterized by a blocky pattern of high P-wave velocity (5000 to 6000 $m.s^{-1}$), whereas the second one, dominated by heterogeneous carbonate facies (F7, F8, F9) shows important vertical variations or porosity (7 to 22 %) and velocity (from 2000 $m.s^{-1}$ up to 6000 $m.s^{-1}$).

The acoustic impedance obviously displays the same vertical trends as the one of $Vp_{in\text{-}situ}$. The resulting reflection coefficient is used to build a synthetic seismic trace that shows a succession of 14 soft-kicks (negative amplitude reflectors in blue) and 15 hard-kicks (positive amplitude reflectors in red). Following the SEG normal convention, the soft kicks correspond to downward decreases of acoustic impedance and negative reflection coefficients, while the hard kicks correspond to downward increases of acoustic impedance and positive reflection coefficients. Indeed, most of the soft kicks are related to downward decreases of $Vp_{in\text{-}situ}$ (S2, S3, S5, S12, S13 and S14; Fig. 10) and several hard kicks are related to downward increases of $Vp_{in\text{-}situ}$ (H1, H2, H3 and H13; Fig. 10). Rapid alternations in acoustic impedance imply a cancellation of the reflection coefficients, resulting in abnormal and attenuated seismic reflectors (*e.g.*, S4, H14, S14; Fig. 10). Furthermore, note that meter-scale levels of $Vp_{in\text{-}situ}$ with homogeneous and blocky pattern may also correspond to attenuated and obliterated seismic reflectors (H4, H5, H6; Fig. 10).

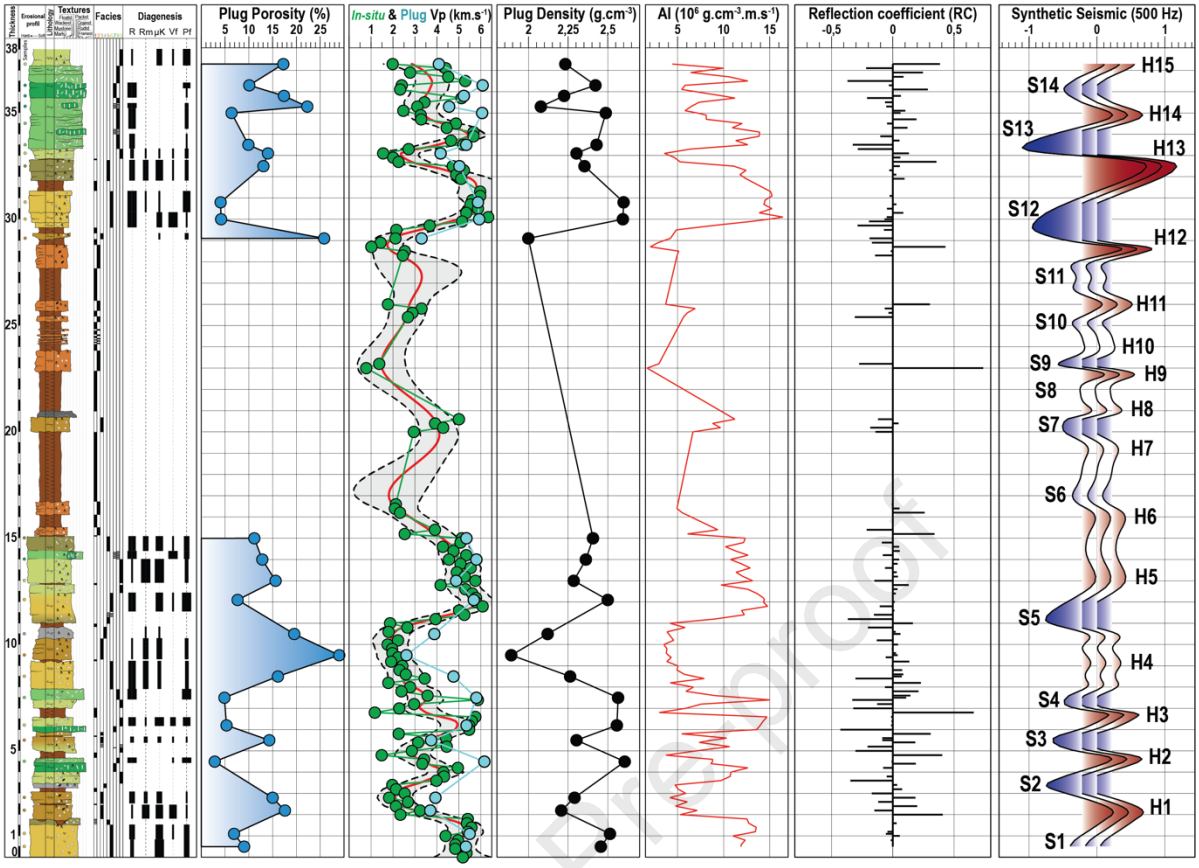

Fig. 10. High resolution seismic stratigraphy of the Marina section. From left to right: Sedimentary log and relative intensity of diagenetic processes (see Fig. 7 for the legend); Plug porosity; P-wave velocity *in situ* (green colour) and plug (blue colour); Plug density; Acoustic impedance; Reflection coefficient; Synthetic seismic. Smooth curves with 95 per cent confidence intervals are indicated for $Vp_{in\text{-}situ}$. The asymmetric shape of reflectors is due to the time-depth conversion.

4.5.2. Antenna section

In the Antenna section, the plug porosity evolution does not show huge vertical variations, being always centred around 2 % to 4 %, with only rare levels of porosity higher than 6 % (e.g., at 6 m, 9 m and 18.6 m; Fig. 11). Most of the plug P-wave velocities fit with the *in-situ* measurements, despite a few levels that show discrepancies between high Vp_{plug} (centred around 5500 $m.s^{-1}$) and lower $Vp_{in\text{-}situ}$ (down to 3000 $m.s^{-1}$).

In the first part of the Antenna section (between 0 m and 11.4 m), $Vp_{in\text{-}situ}$ is globally high (between 5000 $m.s^{-1}$ and 6400 $m.s^{-1}$). It shows only one interval with lower $Vp_{in\text{-}situ}$ values (down to 3000 $m.s^{-1}$) between 6 m and 6.6 m, corresponding to a more porous bed (6,5 % of porosity, facies F5). In the second part of the Antenna section, $Vp_{in\text{-}situ}$ is high between 17 m and 20.2 m, showing values between 5000 $m.s^{-1}$ and 6200 $m.s^{-1}$ with punctual low $Vp_{in\text{-}situ}$ levels at 17.4 and 18.2 m (values around

631 3000 m.s^{-1}). Then, $Vp_{in\text{-}situ}$ presents a more scattered pattern toward the top of the section, with
632 alternating low (down to 3500 m.s^{-1}) and high (up to 5500 m.s^{-1}) values.

633 The synthetic seismic trace of Fig. 11 shows a succession of 6 soft kicks and 6 hard kicks with
634 a much lower amplitude than the one observed on the Marina section (Fig. 10). Indeed, most of the
635 section presents homogeneous and high values of AI without any contrasts of $Vp_{in\text{-}situ}$, implying an
636 attenuation of the reflectors (S1, H1, S2, H3, S4, H4, S6, H6; Fig. 11). Only four reflectors show
637 noticeable amplitude corresponding to high-resolution facies changes (H2, S3, S5 and H5; Fig. 11).
638

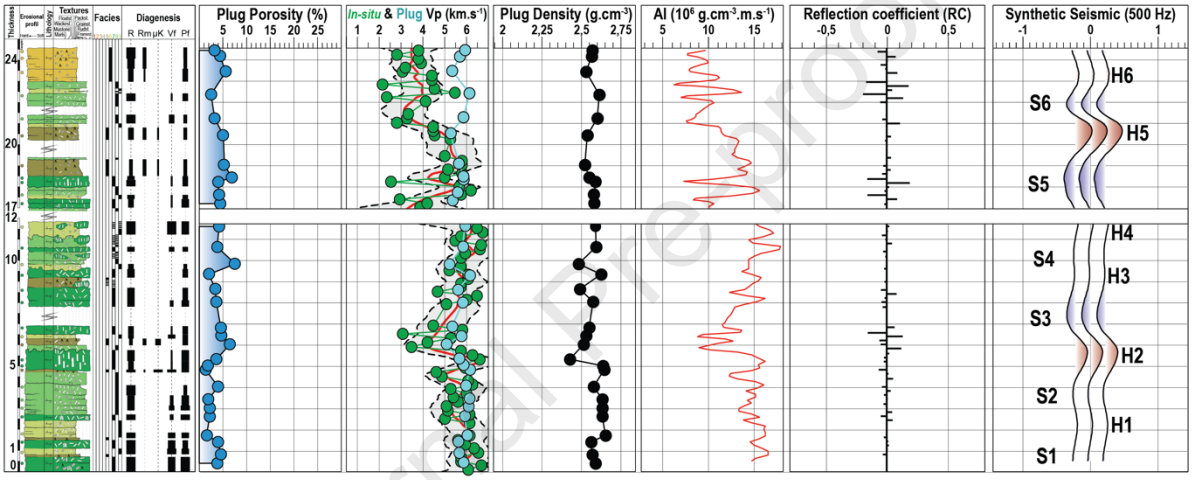

639
640 **Fig. 11.** High resolution seismic stratigraphy of the Antenna section. From left to right: Sedimentary log and
641 relative intensity of diagenetic processes (see Fig. 7 for the legend); Plug porosity; P-wave velocity outcrop (green
642 colour) and plug (blue colour); Plug density; Acoustic impedance; Reflection coefficient; Synthetic seismic.
643 Smooth curves with 95 per cent confidence intervals are indicated for $Vp_{in\text{-}situ}$. The asymmetric shape of reflectors
644 is due to the time-depth conversion.
645

5. Discussion

5.1. Depositional model

Based on the facies definition together with the description of their vertical evolution, a depositional model is proposed (Fig. 12). This model follows partially the studies of Pedley (1990) and Arenas et al. (2007). It is characterized by three coeval domains: alluvial plain (dominated by siliciclastic facies), palustrine (mixed sedimentation) and paludal (pure carbonate sedimentation). The Marina section covers the entire depositional model while the Antenna section mainly represents the paludal domain.

The association of homogeneous reddish to brownish clays (F1) with occasional beds of nodular and marly mudstone (F2) observed in the unit 2 of the Marina section (Fig. 7a) are characteristic of an alluvial plain domain with local ephemeral ponds showing a strong pedogenesis (Fig. 12).

Laterally to this terrestrial domain, a shallow lake is expected (Fig. 12). On its margins, silty pedogenic mudstones to wackestones (F3) dominate, together with peloidal and intraclastic floatstones to packstones (F5). They both show strong evidence of pedogenesis and are grouped into a palustrine domain (Fig. 12). As outlined by Alonso-Zarza (2003), the intraclastic limestones (F5) are the most widespread facies of these environments. Facies F4 (quartz-rich floatstone) is the result of the mixing of quartz-rich sediments coming from the terrestrial domain (fluvial inputs) and reworked carbonate allochems (phytoclasts). Facies F6 (bioclastic packstones and wackestones), characterized by lacustrine biota (*e.g.*, ostracods and gastropods) as well as charophytes, strongly suggests a shallow depositional environment. Indeed, as shown by Asaeda et al. (2007), the optimum development depth of charophytes is comprised between 2 m and 4 m deep. The high occurrence of root traces and exposure surfaces in this facies also point to shallow conditions with episodic exposure and pedogenesis.

The meter-thick levels of phytoherm framestone (F7) correspond to the "vertical tube facies" of Ordóñez and Garcia del Cura (1983), the "phytoherm cushions" of Pedley (1990), or the "phyto-travertine" of Claes et al (2015). According to Pedley (1992), the polycyclic calcitic fringes of phytoherm tufa (Fig. 4d) are due to biomediation processes that allow the phytoherm construction by the *in-situ* growing of low-magnesian calcite cements on the periphery of macrophytes. These coatings allow the preservation of moulds related to macrophytes after the plant decay. Phytoherm framestone

accumulate in a paludal domain (Fig. 12). It follows the definition of Pedley (1990), corresponding to a shallow environment with slow hydrodynamic processes. These deposits are organic-poor as the paludal tufa succession described by Pedley et al. (2003). They settle within a freshwater marsh, with depth ranging from a few decimeters to a few meters (Pedley et al., 2003). They are associated with phytoclastic rudstones (F8) that correspond to the "cross-tube facies" of Ordóñez and Garcia del Cura (1983). This latter facies can have two origins: i) the plant decay, implying a collapse of the phytoherm framestones (Pedley et al., 2003; Pedley, 2009); or ii) a reworking of the phytoherm framestones by flood episodes ("macro detrital tufa" of Ford and Pedley, 1996). Here, the occurrence of erosive bases, oncoids, and reworked phytoclasts within the phytoclastic floatstones (F9) clearly points to episodic higher hydrodynamic conditions in this paludal environment.

As outlined by Heimann and Sass (1996), the paleotopographic setting exerts an important control on the accumulation of such deposits. The succession of palustrine and paludal carbonates of Samos may have accumulated within a low gradient valley fed by freshwaters coming from the neighbouring marble massif (Ampelos nappe of Ring et al., 1999, equivalent of the metamorphic basement shown in Fig. 1a). Such a carbonate source may explain the high degree of saturation with respect to $CaCO_3$ that was necessary for the widespread development of paludal and palustrine facies. The depositional model proposed for the Kokkarion formation of Samos is in part analogous to the "low-gradient, non-stepped fluvial and fluvio-lacustrine" sedimentary facies model of Arenas-Abad et al. (2010).

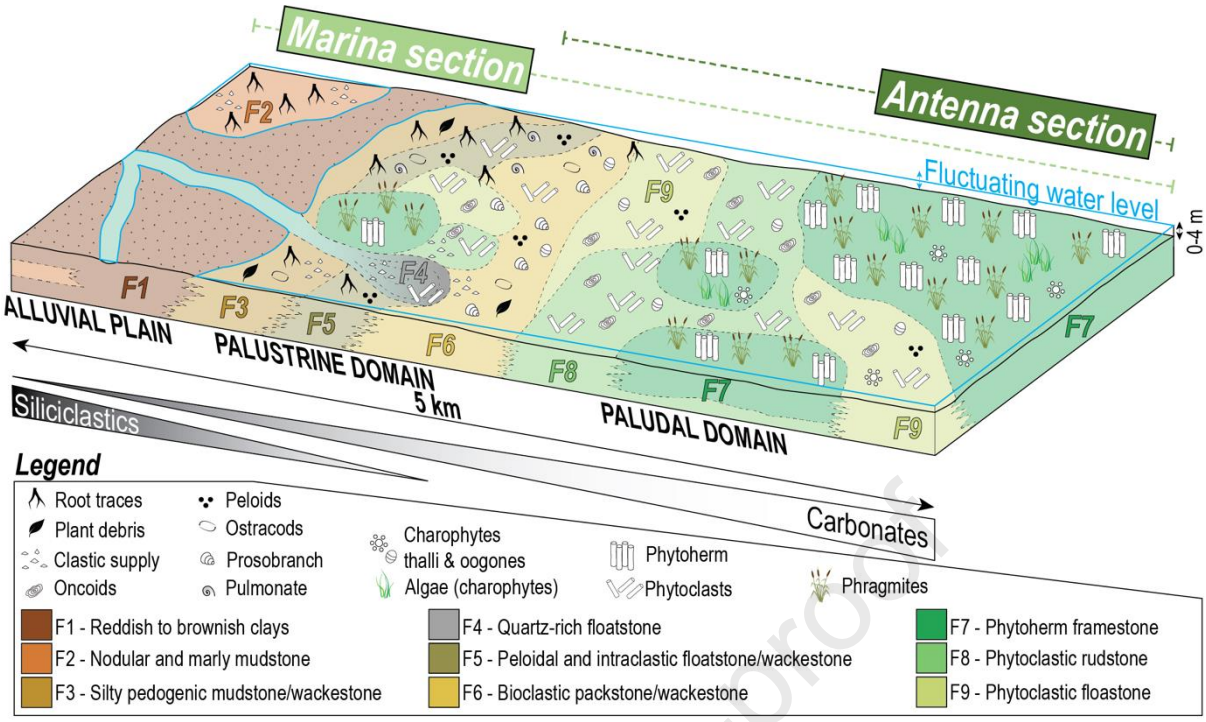

Fig. 12 Depositional model proposed for the Kokkarion fm. of Samos Island.

5.2. Relevance of multi-scale acoustic characterization

Multi-scale characterization of acoustic properties is of importance to understand the geological controlling factors of elasticity in sedimentary rocks and therefore their seismic imaging. In this context, the Pliocene outcropping carbonates from Samos are an ideal target. They show a low amount of burial - in the range of few hundreds of meters - equivalent to the Mio-Pliocene sedimentary systems from SW Turkey (e.g. Çiftçi et al., 2010). Nevertheless, the results acquired on Samos are based on dry acoustic measurements, whereas subsurface reservoirs are fluid saturated (e.g. Fournier et al., 2018). Thus, they are valid in gas saturated reservoirs. In the case of water or oil saturated reservoirs, the velocities obtained in this study should be adjusted by i) correcting the densities and ii) correcting the bulk moduli using Gassmann equation (1951). Note that Gassmann correction is only valid on specific range of frequency, as seismic dispersion and attenuation may occur (e.g. Borgomano et al., 2019, Fortin and Guéguen, 2021).

Furthermore, results of this work show punctual occurrences of $Vp_{in\text{-}situ}$ lower than Vp_{plug} that may be due outcropping root-moulds (Fig. 6a), stem moulds (Fig. 4b) or cracks/fractures. Indeed, as mentioned by Nelson (2001), fractures are pervasively distributed in almost all geological contexts and

may decrease the P-wave velocity of rocks (*e.g.* Boadu and Long, 1996; Matonti et al., 2015, 2017). The differences between *in-situ* and plug velocities can be used to infer a crack/fracture density (Bailly et al. 2019b). However, as highlighted by the Kernel regressions (Figs 10 and 11), the overall vertical evolution of $Vp_{in\text{-}situ}$ mostly mimics the Vp_{plug} evolution. In the case of the Antenna section, the occurrence of punctual lower $Vp_{in\text{-}situ}$ has no effect on the reflection coefficient and thus on the reflectors (Fig. 11). In the case of the Marina section, it is not so straightforward, but most of the reflectors are obtained in domains where the $Vp_{in\text{-}situ}$ are equal to the Vp_{plug} (H1, S2, H2, S3, H3, H4, S5, H5, H6, H12, S12, H13, S13; Fig. 10); i.e. domains without cracks/fractures. Therefore, at the first order, the seismic reflectors obtained in this work are not controlled by structural heterogeneities.

5.3. Sedimentary control of acoustic properties

5.3.1. Facies control on the velocity-porosity relationship at plug scale

As stated by Eberli et al. (2003), the velocity-porosity relationship is crucial for inferring reservoir properties from seismic data. Since the 1950s, several empirical relationships linking these properties have been established (*e.g.*, Wyllie et al., 1956; Anselmetti and Eberli, 1993). Here, the RHG equation (Raymer et al., 1980, Fig. 8a) is used to compare the facies description to a standard petrophysical trend (Fig. 9a and b). Furthermore, the potential impact of facies changes on the seismic reflection are discussed using curves of constant impedances on the velocity-porosity cross-plots as previously proposed in the literature (Anselmetti, 1994; Anselmetti et al., 1997a, 1997b; Anselmetti and Eberli, 2001, Bailly et al., 2019a).

The Marina section offers the opportunity to investigate a huge range of P-wave velocity and porosity. In Fig. 9a, three groups of data can be identified: i) a first group corresponding to high and medium P-wave velocity and porosity fitting with RHG predictions; ii) a second group showing a higher velocity-porosity trend than RHG; and iii) a third group displaying a lower velocity-porosity trend than RHG.

The first group corresponds to intraclastic and peloidal floatstone (F5), bioclastic packstone (F6) and phytoclastic rudstone and floatstone (F8 and F9). These facies mainly deposited in palustrine and paludal

domain, they rarely contain a detrital fraction (Fig. 12). They mostly present a homogeneous texture without any microcracks or heterogeneous macroporosity (Fig. 3f, g, h, Fig. 4h, i), thus explaining the fit with RHG predictions.

The second group is only represented by phytoherm framestones (F7). According to several authors (*e.g.*, Anselmetti, 1994; Eberli et al., 2003; Fortin et al., 2007; Fournier et al., 2014, 2018, Regnet et al., 2019a, 2019b), microstructures with spherical pores might explain these higher values of P-wave velocities. Indeed, the petrographic description showed framework-related macropores inside these samples (Fig. 4e), explaining these peculiar acoustic velocities not predicted by the RHG equation.

The third group of samples corresponds to silty pedogenic mudstones (F3), quartz-rich floatstones (F4) and phytoclastic floatstones (F9). Most of these samples contain abundant siliciclastic material (Fig. 3c, d, e) and were deposited within the palustrine domain, at the transition between the alluvial plain domain and the paludal domain (Fig. 12). According to several authors (Anselmetti et al., 1997b; Kenter et al., 1997, 2007), more than 5 % of siliciclastic content within carbonates decreases the P-wave velocity, thus resulting in a lower velocity-porosity trend than the one predicted by RHG for pure carbonates.

The comparison of the velocity-porosity plot with the facies descriptions helps to understand the scattering of data and distinguish pure versus impure carbonate facies. This point is of importance for seismic modelling because these two sets of data present respectively high and low values of acoustic impedances with a threshold around 10.10^6 $g.cm^3.m.s^{-1}$ (Fig. 9a), that may control the generation of seismic reflectors (Fig. 10). Nevertheless, it does not allow to make distinction between pure carbonate facies (F5, F6, F8 and F9) that do not exhibit peculiar acoustic signatures.

Unlike the Marina section, most of the phytoherm framestones (F7) of the Antenna section fit with the RHG prediction (Fig. 9b). No peculiar distribution of acoustic properties is observed in the light of facies classification. The whole dataset presents low porosity values (< 8 %) and corresponds to pure carbonate facies (F5, F6, F7, F8, F9). This lack of facies control was previously observed for pure carbonate samples (Fournier et al, 2014, Regnet et al., 2015). Here, it results from an absence of detrital content, microcracks or heterogeneous macroporosity. Furthermore, the curves of constant impedance

769 only correspond to high values of AI (between 13.10^6 g.cm^3.m.s^{-1} and 17.10^6 g.cm^3.m.s^{-1}), thus
770 questioning the implication of facies changes in the seismic modelling of this section (Fig. 11).
771
772 *5.3.2. Facies control of* in-situ *acoustic measurements*
773 Based on $Vp_{in\text{-}situ}$ and the sedimentary description, a statistical view of the data is provided per
774 facies, using violin plots (Fig. 9c and d). Such *in-situ* acoustic measurements have already been proposed
775 to characterize fractured outcrops (Jeanne et al., 2012; Matonti et al., 2015) and for upscaling purposes
776 (Bailly et al., 2019b). Here, this approach aims to obtain a large set of data representative of a scale
777 higher than the conventional plug scale while discussing about the facies control.
778 In the Marina section, the low values of P-wave velocities observed for F1, F2, F3 or F4 are
779 analogous to literature data for such detrital-rich facies (Bourbié et al., 1987). These results are similar
780 to the laboratory dataset (Fig. 9a), outlining again the impact of detrital content on the acoustic
781 properties. The acoustic contrast between F1 values (lower than 1500 m.s-1) and F2, F3 or F4 values
782 (from 2000 to 3000 m.s-1) may imply possible seismic reflection. As previously presented, two groups
783 of carbonate facies can be defined, based on their P-wave velocities. The higher velocities observed for
784 facies F5 and F6 can be explained by a rather homogeneous composition (Fig. 3f, g, h), without any
785 large-scale heterogeneities (*i.e.* absence of macroporosity). On the opposite, the lower values and the
786 important scattering of the P-wave velocities for the carbonate facies F7, F8 and F9 suggest outcrop-
787 scale heterogeneities, such as macropores related to phytoherm and phytoclastic facies (Fig. 4a, b, e, g).
788 Consequently, the lower P-wave velocity values (< 4000 m.s^{-1}, Fig. 9c) of phytoherm framestones (F7)
789 and phytoclastic floatstones and rudstones (F8 and F9) may create contrasts with higher P-wave
790 velocities (> 4000 m.s^{-1}, Fig. 9c) of pure carbonate facies (F5, F6, and to a lower extent F7, F8 and F9).
791 This point is not observed with the laboratory dataset, where the pure carbonate facies (F5, F6, F7, F8
792 and F9) are always associated with high P-wave velocities (> 4000 m.s^{-1}; Fig. 9a).
793 For the facies F5, F7, F8 and F9 of the Antenna section, the median values of the *in-situ* P-wave
794 velocities are all comprised between 5000 and 6000 m.s^{-1} (Fig. 9d), in line with the laboratory dataset
795 values (Fig. 9b). This observation suggests a lack of facies control on the acoustic properties, except for
796 the bioclastic packstone where the median of the *in-situ* P-wave velocity is lower than 4000 m.s^{-1} (F6,

797 Fig. 9d).This points to a possible scale effect and a potential impact of heterogeneities that are not
798 characterized at the laboratory scale (Matonti et al., 2015; Bailly et al., 2019b), here most probably
799 related to the occurrences of root networks that are highly developed at the top of the Antenna section
800 (Figs 6b, 7b and 11).
801
802 To summarize, the facies variation can explain the wide range of acoustic velocities acquired
803 on the Marina section. However, similar facies occurring in the Antenna section show very small
804 variations of P-wave velocity. As a consequence, the sole sedimentological description is not enough to
805 understand the distribution of acoustic properties in these carbonates.
806
807 *5.4. Impact of early diagenesis on acoustic and seismic properties*
808 We compare the velocity-porosity datasets with diagenesis for palustrine and paludal carbonates
809 (Figs 13 and 14). Four main diagenetic overprints and related pore types are defined, describing the
810 velocity-porosity data: i) pervasive recrystallization and blocky cementation (Figs 13a, b and 14a, b, d);
811 ii) preserved root moulds showing a pore-lining cement (Figs 13a, c and 14a, f); iii) preserved
812 heterogeneous macroporosity (Fig. 14a, c); iv) microporous host containing cemented root-moulds (Fig.
813 13a, d) and showing evidence of recrystallization (Fig. 14a, e). Following the allochem content
814 (ostracods, polycyclic calcite sheets of tufas…), and the crystal morphology of micrite, we assume that
815 the primary mineralogy of the carbonate mostly corresponds to low magnesian calcite (*e.g.* Capezzuolli
816 et al., 2014).
817 The paragenetic sequences (Fig. 5) show that an intense to pervasive phase of recrystallization
818 together with a subsequent phase of granular to blocky calcite cementation (Fig. 6f-j) affect some pure
819 carbonate samples (F5, F6, F7, F8, F9), especially for the Antenna section (Figs 5b, 7b, 11). Conversely,
820 in the Marina section, these diagenetic processes are less intense and occur more sporadically (Figs 5a,
821 7a and 10). The SEM investigations of some recrystallized samples from the Antenna section display a
822 fused micrite associated with P-wave velocity matching the RHG prediction (Fig. 14a, d). Other samples
823 show a preserved microporosity, with a subrounded micrite showing small, rounded crystals (<2 µm)
824 embedded within larger overgrowth crystals (>4 µm), associated with a P-wave velocity slightly lower

than RHG prediction (Fig. 14a, e). Such morphologies are a typical result of the Ostwald ripening process that occurs during meteoric diagenesis in a phreatic setting (Volery et al., 2010). This process allows the dissolution of the smallest and most unstable crystals, thus favouring the overgrowth of the larger crystals (Fig. 14e). The different process intensities between fully recrystallized samples (fused micrite, Fig. 14d) and partially microporous samples (subrounded micrite, Fig 13e) can be explained by the residence time of the rocks in a phreatic meteoric environment oversaturated with respect to $CaCO_3$: the longer the time is, the stronger the recrystallization and cementation are. Furthermore, given the described depositional textures (especially F7 and F8), the relatively high primary porosity of the studied palustrine and paludal tufa carbonates would have provided a good primary permeability allowing fluid infiltration (De Boever et al., 2017) and a high diagenetic precipitation potential.

Pervasive recrystallization and cementation are thus proposed to be the main drivers of the porosity/velocity signatures in the Kokkarion formation. These diagenetic processes built a rigid framework and occluded pore space, which results in P-wave velocities averaging 6000 $m.s^{-1}$, porosity values comprised between 2 to 5% and very high acoustic impedance values (mostly higher than 14.10^6 $g.cm^3.m.s^{-1}$ (Figs 13a and 14a). In the Antenna section, samples only partially recrystallized (subrounded micrite, partial preservation of microporosity, Fig. 14a, e) show slightly higher porosity (6%) and lower velocity (5300 $m.s^{-1}$), with still high acoustic impedance (13.10^6 $g.cm^3.m.s^{-1}$). However, they are not associated with a large range of porosity and velocity, as observed in the Marina section (low AI values, down to 5.10^6 $g.cm^3.m.s^{-1}$, Fig. 13a). Indeed, some samples of the Marina section present root-related moulds (Fig. 13c) and high microporosity (Fig. 13d), resulting in P-wave velocity values lower than 5500 $m.s^{-1}$ and porosities higher than 10 % (Fig. 13a). Hence, the occurrence of microporosity may imply P-wave velocities lower than non-microporous rocks, thus obstructing wave propagation in carbonates ("softening effect" *sensu* Xu and Payne, 2009, Zhao et al., 2013, see also Eberli et al., 2003; Baechle et al., 2008; Fournier et al., 2011). We can also notice the occurrence of pore-lining cement filling root moulds of some microporous samples (Figs. 13c and 14f). Such a cement rigidifies the microporous samples ("stiffening effect" *sensu* Xu and Payne, 2009, Zhao et al., 2013), inducing P-wave velocities matching the RHG prediction and resulting in intermediate AI values centred around 12.10^6 $g.cm^3.m.s^{-1}$ (Figs 13a and 14a). Finally, for the phytoherm framestone (F7) and

853 phytoclastic rudstone (F8), even if the preserved macropores result in medium to high porosities
854 (between 6 % and 23 %), high to moderate values of P-wave velocities are observed (between 6000 $m.s^{-1}$
855 and 4500 $m.s^{-1}$), higher than RHG prediction (Fig. 14a, c). Indeed, the preservation of heterogeneous
856 macropores, due to the absence of blocky cementation, induces a stiffening of the microstructure and
857 controls the acoustic properties of phytoherm framestone and phytoclastic rudstone (Fig. 14a, c),
858 mimicking the acoustic behaviour of mould-rich carbonates (*e.g.* Eberli et al., 2003; Soete et al., 2015).
859 The variation of this porosity is responsible of the high fluctuation of *in-situ* P-wave velocity in the
860 Marina section (Fig. 10).

861 In summary, the Marina section displays large differences in the diagenetic processes
862 overprinting the facies heterogeneities, resulting in a large range of acoustic impedance. In contrast, the
863 Antenna section only shows high values (with minor variations) of acoustic impedance, due to a
864 pervasive recrystallization and cementation of the whole sedimentary section.
865

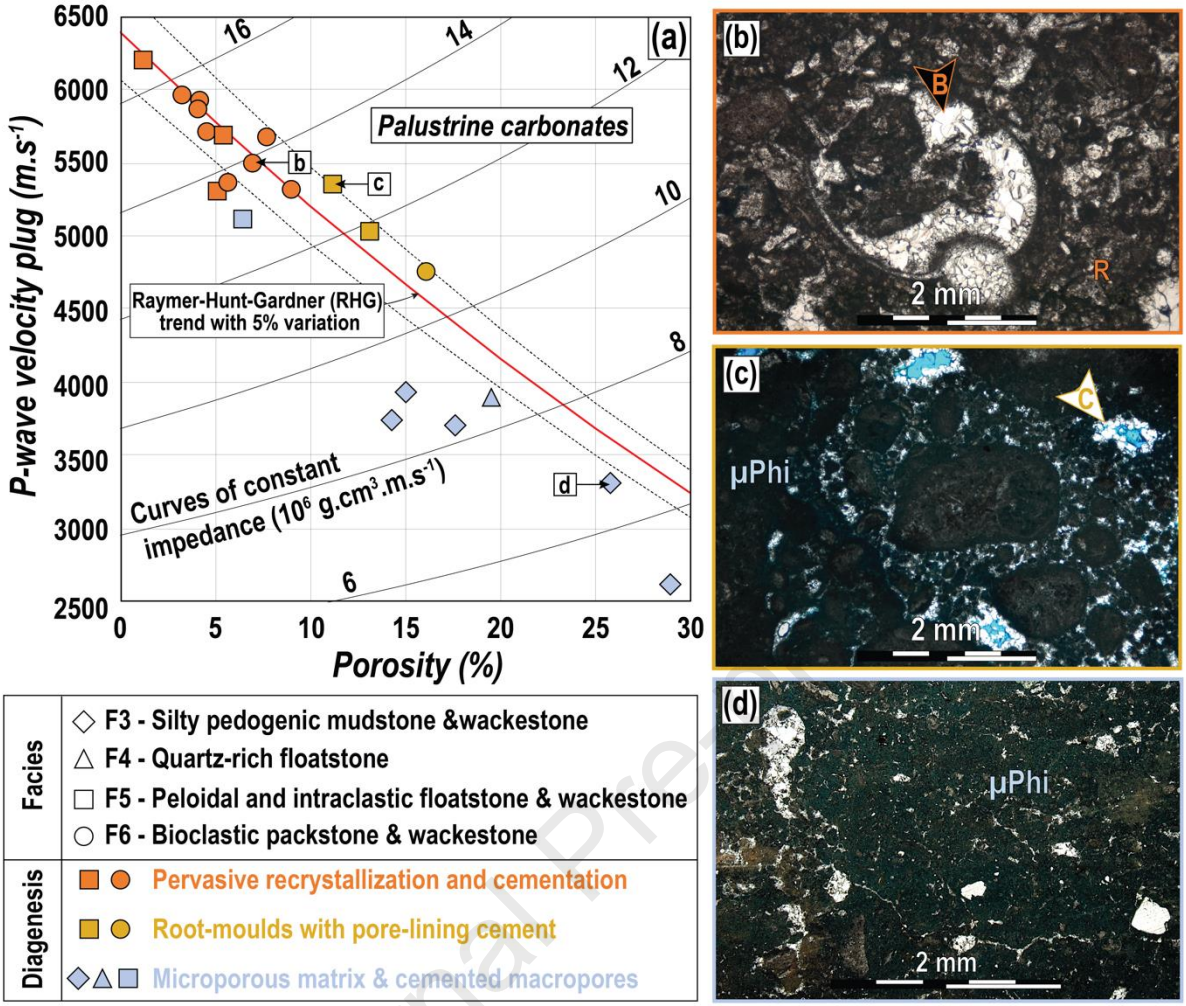

Fig. 13. Diagenetic control of acoustic and seismic properties in palustrine carbonates. The colors used to frame the pictures refers to the colors used in the crossplot. (a) P-wave velocity versus porosity sorted per facies and diagenesis; (b) PPL view of a recrystallized (R) bioclastic packstone showing primary intragranular porosity filled by a blocky cement (B); (c) PPL view of a microporous (µPhi) intraclastic wackestone showing a pore-lining cementation (C) in residual root-moulds; (d) PPL view of a microporous (µPhi) micritic matrix of a silty pedogenic wackestone.

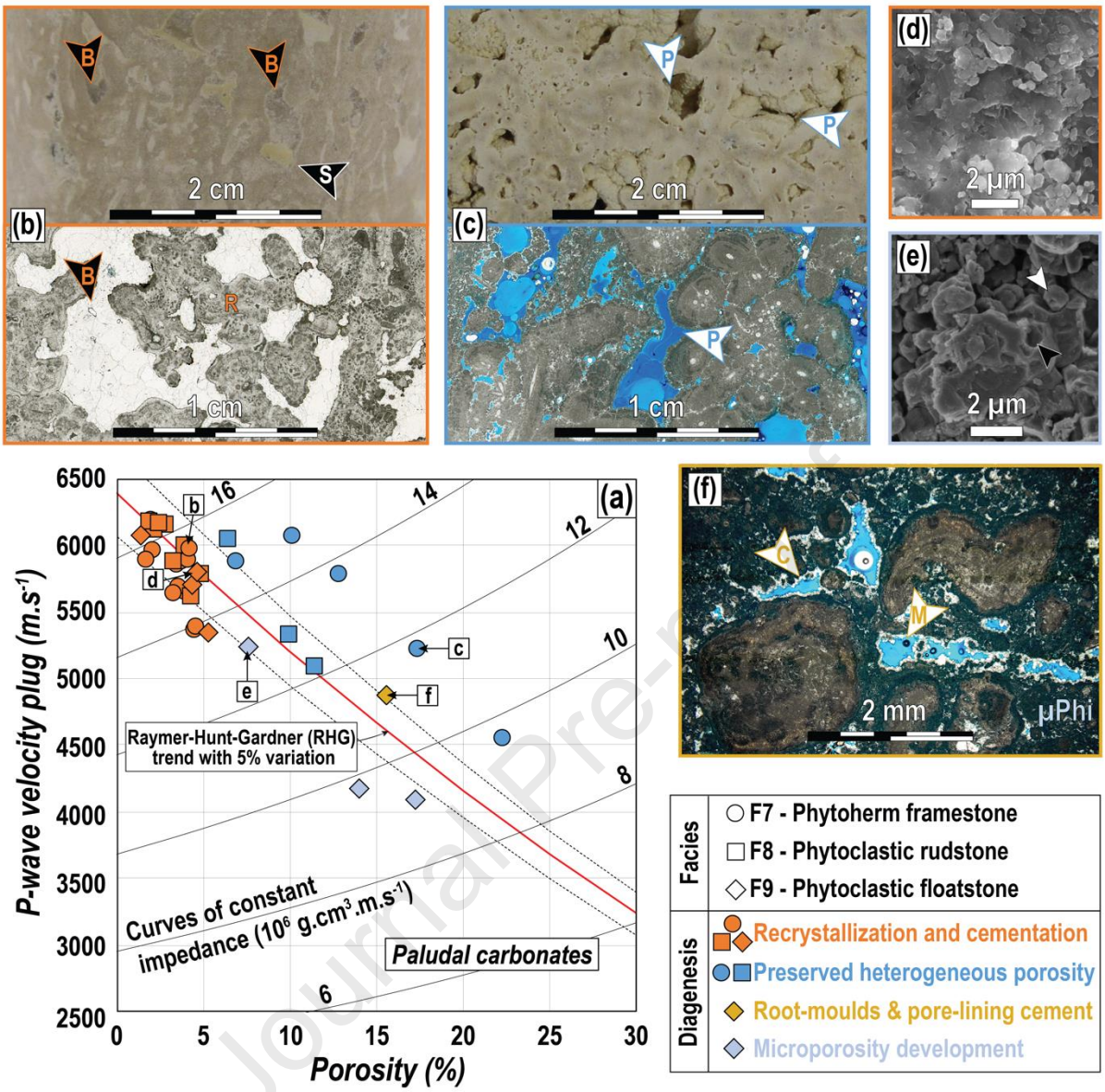

Fig. 14. Diagenetic control of acoustic and seismic properties in paludal carbonates. The colors used to frame the pictures refers to the colors used in the crossplot. (a) P-wave velocity versus porosity sorted per facies and diagenesis; (b) Macroscopic and PPL views of a recrystallized (R) phytoherm framestone, with primary macropores filled with blocky cement (B) and with vadose silts (S); (c) Macroscopic and PPL views of a macroporous phytoherm framestone with preserved primary macropores (P); (d) SEM view of a fused micrite; (e) SEM view of a subrounded porous micrite, showing small rounded crystals (white arrow) embedded within larger overgrowths (black arrow); (f) PPL view of a microporous (µPhi) phytoclastic floatstone showing root moulds (M) partly filled by a pore-lining cement (C).

5.5. Significance of high-resolution seismic reflectors in palustrine and paludal tufa carbonates

5.5.1. Combined control of sedimentary facies and early diagenesis

As introduced in Fig. 10, a series of well-developed seismic reflectors was recognized and compared to the sedimentary succession of the Marina section. Most of these reflectors correspond to facies changes. It also appears that some reflectors are linked to contrasts of diagenesis, with differential recrystallization/cementation. This is summarized in the green box of the Fig. 15a: i) the high amplitude soft kick (S13 on Fig. 10) represents a contrast between overlying moderately to intensely recrystallized/cemented bed of phytoclastic rudstone (F8) and underlying lowly recrystallized/cemented bed of phytoclastic floatstone (F9); while ii) the high amplitude hard kick (H13 on Fig. 10) fits with a contrast between overlying lowly recrystallized/cemented bed of phytoclastic floatstone (F9) and underlying moderately to intensely recrystallized/cemented bed of peloidal and intraclastic floastone (F5). As a consequence, the high amplitude seismic reflectors within palustrine and paludal tufa carbonates mainly correspond to vertical variations of facies overprinted by differential diagenesis, which is consistent with the findings of Bailly et al. (2019a) on lacustrine and palustrine carbonates. These results are also in line with the work of Teillet et al. (2020) who argued that vertical changes in facies without differential diagenetic evolution cannot create reflectors (conventional seismic, frequency of 45 Hz, resolution of 20 meters).

5.5.2. Impact of diagenetic homogenization

Diagenetic homogenization can obliterate the seismic signal, resulting in reflection free zones (*sensu* Mitchum et al., 1977), as exemplified on the Antenna section where the acoustic impedance is rather homogeneous (Fig. 11). This is entirely due to an overall high intensity of recrystallization and cementation (Fig. 14a, b) that erased all the potential contrasts associated to vertical facies variations (red box on Fig. 15b), resulting only in high AI. Following our dataset, such erasing of geological contrasts may also be due to a pervasive pedogenesis and a low meteoric phreatic cementation (Marina section, reflector H4 on Fig. 10). It results in the preservation of root moulds within meter-thick succession of microporous silty pedogenic mudstone (F3) and bioclastic packstone (F6). In these contexts, the absence of seismic reflectors is thus related to the vertical homogeneity of the porosity

values inducing a blocky pattern of the P-wave velocity variation, itself explained by: i) a cemented and recrystallized succession of pure carbonates or ii) a pedogenic microporous succession of pure and impure carbonates. Such high-resolution reflection free-zone in continental carbonates (here up to 20 meters-thick, Antenna section, Fig. 11) is analogous to the "seismodiagenetic units" defined by Fournier and Borgomano (2007) or the "petroacoustic groups" of Teillet et al. (2020) for marine carbonates. Indeed, these "units" or "groups" correspond to decameter-thick successions of various facies overprinted by a given diagenetic signature, equivalent to the diagenetic homogenization of the Antenna section responsible of the reflection free-zone's formation. Consequently, those findings are likely suggesting a crucial diagenetic control on seismic reflection in paludal and palustrine carbonates.

5.5.3. Heterogeneous facies and low diagenetic contrasts

As highlighted by the blue box in the Fig. 15a, low amplitude seismic reflectors occur within the heterogeneous facies succession (F7 and F8, H14 and S14 of Fig. 10). Such a signal is explained by the high vertical contrast of acoustic impedance induced by the rapid succession of beds with high contrasts of P-wave velocity signature (as outlined by the violin plots of F7, F8 and F9, Fig. 9d). It is analogous to the "destructive interfering waves" phenomena proposed by Jafarian et al. (2018). Furthermore, the diagenetic characterization of these heterogeneous carbonates shows a high intensity of recrystallization together with a moderate cementation, pointing to a lack of diagenetic contrast (blue box on Fig. 15a). These beds show a preserved macroporosity, resulting from a combined control of sedimentological heterogeneity (genesis of primary macroporosity) and diagenetic evolution (low cementation). As a consequence, succession of low amplitude seismic reflectors amongst high amplitude reflectors may point to heterogeneous and macroporous carbonates. Additionally, other low amplitude seismic reflectors occur within the Antenna section, (H2, S5 and H5 on the Fig. 11). In these cases, they are rather associated to vertical facies variations with low diagenetic contrasts (blue box of Fig. 15b) occurring amongst a global reflection free zone. Therefore, the interpretation of low amplitude seismic reflectors in paludal and palustrine tufa carbonates need to be done with care given that they may correspond either to a heterogeneous porous succession (blue box of Fig. 15a) or to a low porous succession (blue box of Fig. 15b).

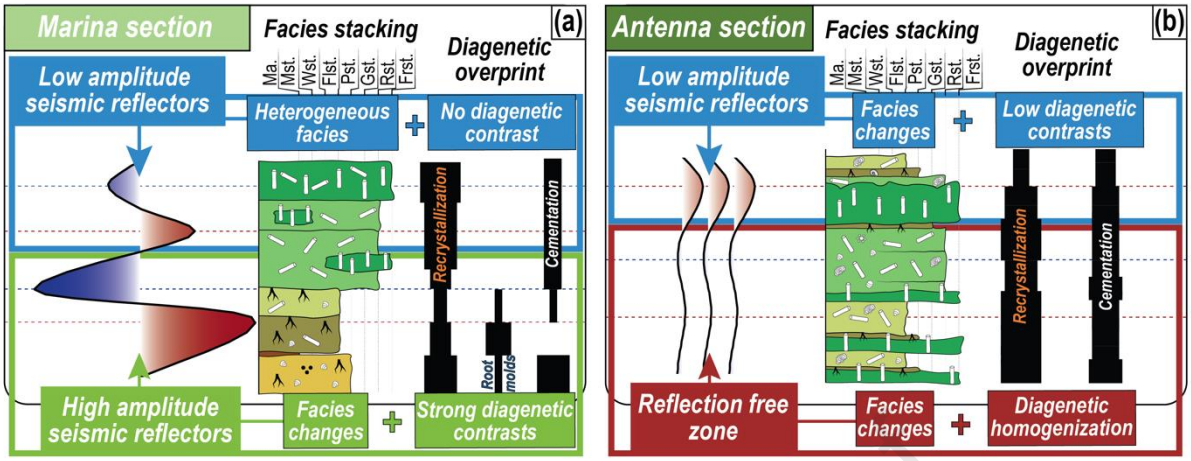

Fig. 15. Geological significance of high-resolution reflectors in palustrine and paludal tufa carbonates: (a) Examples of well-developed seismic reflectors (green box) and low amplitude seismic reflectors (blue box) in the Marina section; (b) Examples of obliterated seismic reflectors (red box) and low amplitude seismic reflectors (blue box) in the Antenna section. The facies stacking and diagenetic overprint are simplified from Figs 10 and 11.

5.6. Acoustic and seismic properties of continental carbonates, contribution of our dataset

Figure 16 compares our laboratory dataset with available literature data of continental carbonates: i) outcropping Miocene lacustrine and palustrine carbonates from Samos Island, Greece (Bailly et al. 2019a, Fig. 16a; top Hora formation on Fig. 1a, b); ii) outcropping Quaternary travertine from Turkey and Hungary (Soete et al., 2015, Fig. 16b); iii) outcropping Miocene alluvial to lacustrine carbonates from Madrid Basin, Central Spain (Reijmer et al., 2021, Fig. 16b); iv) outcropping and subsurface analogs of presalt carbonates (Regnet et al., 2019a, Fig. 16b); and v) subsurface Lower Cretaceous presalt carbonates from Santos Basin, offshore Brazil (Vasquez et al., 2019, Fig. 16b). Note that all the data of the Fig. 16 were acquired under dry conditions, therefore solely controlled by microstructural heterogeneities and not influenced by fluid-induced velocity dispersion (e.g. Borgomano et al., 2019). Furthermore, the acoustic data of samples from Samos are fairly consistent with other acoustic datasets, although the pressure conditions of the measurements are not similar (~0.1 MPa for Fig. 16a ; 27.6 MPa to 40 MPa for Fig. 16b).

A first striking feature from the Fig. 16 is the well-known impact of siliciclastic content on the acoustic properties that greatly reduce the P-wave velocity for a given porosity (Anselmetti et al., 1997b, Kenter et al., 1997, 2007, Reijmer et al., 2021). On the opposite, the occurrence of stiff pores within pure carbonate hosts (*e.g.* stem-moulds, ooid-moulds, bio-moulds, vugs and framework porosity, Fig.

16) significantly increase the P-wave velocity for a given porosity (e.g. Eberli et al., 2003, Fournier et al., 2018, Bailly et al., 2019a, Jaballah et al., 2021, Matonti et al., 2021, Salih et al., 2021). Consequently, the heterogeneities of both mineralogy and porous networks strongly control the acoustic impedance (AI) of continental carbonates and therefore seismic. As an example, for a porosity of 10 %, AI contrasts between stem mould-rich tufa carbonates (15.10^6 $g.cm^3.m.s^{-1}$; Fig. 16a) and siliciclastic-rich carbonates (9.10^6 $g.cm^3.m.s^{-1}$; Fig. 16b) can create seismic reflectors, reflecting the depositional environment control. Conversely, for pure calcite rocks, AI contrasts between highly cemented and recrystallized carbonates (16.10^6 $g.cm^3.m.s^{-1}$; Fig. 16a) and ooid mould-rich or vug-rich carbonates (8.10^6 $g.cm^3.m.s^{-1;}$; Fig. 16a, b) can also create reflectors, outlining here a diagenetic control. However, for AI in the range of 8-10.10^6 $g.cm^3.m.s^{-1}$, seismic cannot depict contrasts between poorly porous siliciclastic-rich carbonates and highly porous carbonates with moulds, vugs and framework porosity (Fig. 16b), making difficult the imaging of such a continental carbonate succession.

Another essential controlling parameter of acoustic and seismic properties of continental carbonates is their primary mineralogy. Indeed, continental depositional environments can induce the precipitation of i) stable LMC (e.g. paludal tufa of Kokkarion Formation of Samos) and ii) unstable HMC and/or aragonite (e.g. oolitic grainstones of Hora formation of Samos, Bailly et al., 2019a). Such mineralogical heterogeneities are responsible of two distinct diagenetic trends controlling the acoustic and seismic properties: i) the stable mineralogy of paludal tufa carbonates inhibited subsequent dissolution processes while cementation and recrystallization processes induced a decrease of the primary porosity and an increasing P-wave velocity (Fig. 16a). On the opposite: ii) the unstable mineralogy of lacustrine oolitic grainstones controlled their dissolution potential, resulting in high secondary porosity and low P-wave velocity (Fig. 16a). Such considerations are analogous to the findings of Anselmetti and Eberli (1993) and Matonti et al. (2021) who also point out the control of initial mineralogy on the diagenetic potential of marine carbonates and their resulting acoustic properties.

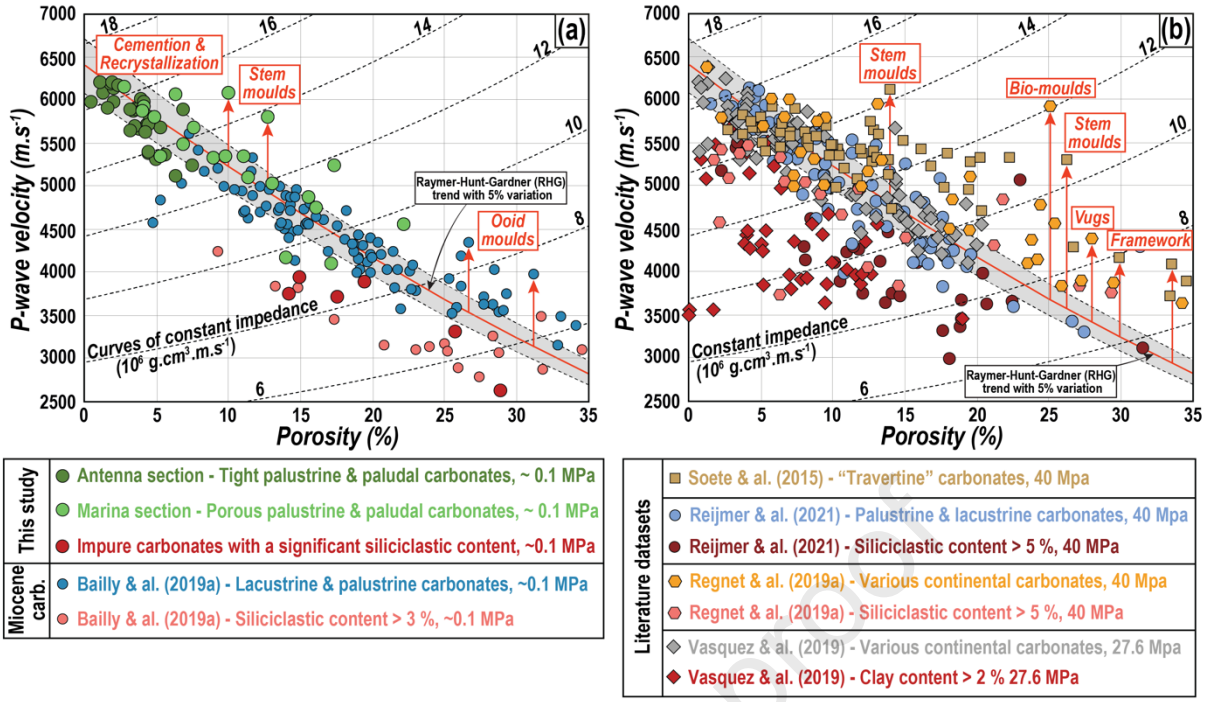

Fig. 16. Compilation of P-wave velocity and porosity data of continental carbonates. The vertical red arrows point to samples showing a distinctive porous network explaining the positive deviation from the RHG equation. (a) Comparison of our dataset with the data of Bailly et al. (2019a). The acoustic measurements were acquired under dry conditions with a very low pressure. (b) Comparison of the datasets provided by Soete et al. (2015), Reijmer et al. (2021), Regnet et al. (2019a), and Vasquez et al. (2019). The acoustic measurements were acquired under dry conditions with a high confining pressure (40 MPa, 27.6 MPa). Note that our samples and the one of Bailly et al. (2019a) and Soete et al. (2015) are quasi-pure carbonates, containing only calcite with a small siliciclastic amount. Samples of Regnet et al. (2019a) are composed of calcite, dolomite and a variable siliciclastic content (quartz and clays). Samples of Vasquez et al. (2019) are composed of calcite, dolomite, quartz and a variable amount of clays. Samples of Reijmer et al. (2021) are composed of calcite and a variable siliciclastic content (quartz, clays and plagioclase).

6. Conclusions

In this work, the acoustic and seismic properties of two sedimentary successions of palustrine and paludal carbonates are discussed. An extensive petrographic characterization enabled to define nine facies affected by several diagenetic processes acting in a meteoric realm. According to the vertical facies variations, a depositional model corresponding to a low gradient valley fed by freshwaters is proposed. Combining geological observations with i) a field and laboratory investigation of acoustic properties, and ii) 1D synthetic seismic modelling of two studied sections lead to the following conclusions. At the plug scale, facies and early diagenetic overprint control the acoustic properties. At the outcrop scale, the sole facies variation does not explain the acoustic properties evolution. Indeed, despite the two studied section display similar sedimentary facies, their seismic responses are distinctive, mostly due to a diagenetic control:

(1) Geological contrasts corresponding to vertical changes of facies combined with diagenetic contrasts lead to the development of high amplitude seismic reflectors;

(2) Vertical facies variations overprinted by an extensive diagenetic homogenization correspond to reflection free zones;

(3) Vertical facies variations combined with low diagenetic contrasts and vertical succession of heterogeneous porous facies are associated with low amplitude seismic reflectors.

These conclusions demonstrate the sedimentary and diagenetic controls of seismic properties in palustrine and paludal tufa. Such geological controlling factors are of primary importance to understand the reservoir compartmentalization of heterogeneous carbonates using crosswell seismic imaging.

Acknowledgments

This work was supported by IFP Energies Nouvelles (grant XFP32/001). It is a part of the PhD project of the first author, at IFP Energies Nouvelles and Laboratoire de Géologie of Ecole normale supérieure, as well as the master thesis of the second author. We thank Phillippe Blanc (society Lithologie Bourgogne) for the preparation of the thin sections, Damien Deldicque (ENS) for the SEM observations and Nicholas Badullovich for the English proofreading of this article. We acknowledge John J. G. Reijmer and two anonymous reviewers for their constructive comments which helped to improve this manuscript. We also thank the associate editor Telm Bover-Arnal.

References

Al-Chalabi, M., 2014. Principles of Seismic Velocities and Time-to-Depth Conversion, EAGE Publications.

Alonso-Zarza, A.M., 2003. Palaeoenvironmental significance of palustrine carbonates and calcretes in the geological record. Earth-Sciences Reviews 60, 261–298. https://doi.org/10.1016/S0012-8252(02)00106-X

Alonso-Zarza A.M., Tanner L.H., 2010a. Carbonates in continental settings: Facies, environments and processes, Developments in Sedimentology, 61, Elsevier.

1041 Alonso-Zarza A.M., Tanner L.H., 2010b. Carbonates in continental settings: Geochemistry, diagenesis
1042 and applications, Developments in Sedimentology, 62, Elsevier.
1043 Anselmetti, F.S., Eberli, G.P., 1993. Controls on Sonic Velocity in Carbonates, in: Liebermann, R.C.,
1044 Sondergeld, C.H. (Eds.), Experimental Techniques in Mineral: The Shreiber Volume, pp. 287 –323.
1045 Anselmetti, F.S. (1994). Physical properties and seismic response of carbonate sediments and rocks,
1046 Ph.D Thesis, ETH Zürich.
1047 Anselmetti, F.S., Eberli, G.P., Bernouilli, D., 1997a. Seismic Modeling of Carbonate Platform Margin
1048 (Montagna della Maiella, Italy): Variations in Seismic Facies and Implications for Sequence
1049 Stratigraphy, in: Palaz, I, Marfurt, K.J., (Eds.), Carbonate Seismology: Geophysical Developments.
1050 Society of Exploration Geophysicists, Tulsa, Oklahoma, pp. 373–406.
1051 Anselmetti, F.S., Von Salk, G.A., Cunningham, K.J., Eberli, G.P., 1997b. Acoustic properties of
1052 Neogene carbonates and siliciclastics from the subsurface of the Florida Keys: implications for seismic
1053 reflectivity. Marine Geology 144, 9–31. https://doi.org/10.1016/S0025-3227(97)00081-9
1054 Anselmetti, F.S., Eberli, G.P., 2001. Sonic velocity in carbonates – A combined product of depositional
1055 lithology and diagenetic alterations. SEPM Special Publication 70, 193–216.
1056 https://doi.org/10.2110/pec.01.70.0193
1057 Antonelli, M., Miranda, F., Terzi, L., Valenti, G., 2004. Integrated crosswell seismic: Case histories in
1058 advanced technology to improve reservoir description. First Break 22, 49–56.
1059 https://doi.org/10.3997/1365-2397.22.5.25900
1060 Arenas, C., Cabrera, L., Ramos, E., 2007. Sedimentology of tufa facies and continental microbialites
1061 from the Palaeogene of Mallorca Island (Spain). Sedimentary Geology 197, 1–27.
1062 10.1016/j.sedgeo.2006.08.009
1063 Arenas-Abad, C., Vàzquez-Urbez, M., Pardo-Tirapu, G., Sancho-Marcén, C., 2010. Fluvial and
1064 Associated Carbonate Deposits, in: Alonso-Zarza, A.M., Tanner, L.H. (Eds.), Carbonates in Continental
1065 Settings: Facies, Environments, and Processes, Vol. 61, Elsevier, pp. 133–175.
1066 Armenteros, I., 2010. Diagenesis of Carbonates in Continental Settings, in: Alonso-Zarza A.M., Tanner
1067 L.H. (Eds.), Carbonates in continental settings: Geochemistry, diagenesis and applications,
1068 Developments in sedimentology, vol. 62, Elsevier, pp. 61–151.

1069 Asaeda, T., Rajapakse, L., Sanderson, B., 2007. Morphological and reproductive acclimations to growth
1070 of two charophyte species in shallow and deep water. Aquatic Botany 86(4), 393−401.
1071 10.1016/j.aquabot.2007.01.010
1072 Baechle, G.T., Colpaert, A., Eberli, G.P., Weger, R.J., 2008. Effect of microporosity on sonic velocity
1073 in carbonate rocks. The Leading Edge 17, 1012–1018. https://doi.org/10.1190/1.2967554
1074 Bailly, C., Adelinet, M., Hamon, Y., Fortin, J., 2019a. Combined control of sedimentology and
1075 diagenesis on seismic properties in lacustrine and palustrine carbonates (Upper Miocene, Samos Island,
1076 Greece). Geophysical Journal International 219, 1300–1315. https://doi.org/10.1093/gji/ggz365
1077 Bailly, C., Fortin, J., Adelinet, M., Hamon, Y., 2019b. Upscaling of Elastic Properties in Carbonates: a
1078 Modelling Approach Based on a Multiscale Geophysical Data Set. Journal of Geophysical Research:
1079 Solid Earth 124(12), 13021–13038. https://doi.org/10.1029/2019JB018391
1080 Bear, J., 1972. Dynamics of Fluids in Porous Media, American Elsevier Publishing Compagny, New
1081 York.
1082 Boadu, F.K., Long, L.T., 1996. Effects of fractures on seismic-wave velocity and attenuation.
1083 Geophysical Journal International 127, 86–110. https://doi.org/10.1111/j.1365-246X.1996.tb01537.x
1084 Bourbié, T., Coussy, O., Zinszner, B., 1987. Acoustics of Porous Media. Editions Technip, Paris.
1085 Beavington-Penney, S.J., Wright, V.P., Barnett, A., Kennedy, S., 2019. Integration of static and dynamic
1086 data and high-resolution sequence stratigraphy to define reservoir architecture and flow units within a
1087 'super giant' gas condensate and oil field, Kazakhstan. Marine and Petroleum Geology 101, 486–501.
1088 https://doi.org/10.1016/j.marpetgeo.2018.11.005
1089 Borgomano, J.V.M., Pimienta, L.X., Fortin, J., Guéguen, Y., 2019. Seismic Dispersion and Attenuation
1090 in Fluid-Saturated Carbonate Rocks : Effect of Microstructure and Pressure. Journal of Geophysical
1091 Research: Solid Earth 124(12), 12498–12522. https://doi.org/10.1029/2019JB018434
1092 Brigaud, B., Vincent, B., Durlet, C., Deconinck, J., Landrein, P., Jobard, E., Pickard, N., 2014.
1093 Characterization and origin of permeability-porosity heterogeneity in shallow-marine carbonates : From
1094 core scale to 3D reservoir dimension (Middle Jurassic, Paris Basin, France). Marine and Petroleum
1095 Geology 57, 631–651. https://doi.org/10.1016/j.marpetgeo.2014.07.004

1096 Capezzuoli, E., Gandin, A., Pedley, M., 2014. Decoding tufa and travertine (fresh water carbonates) in
1097 the sedimentary record: The state of the art. Sedimentology 61, 1–21. https://doi.org/10.1111/sed.12075
1098 Choquette, P.W., Pray, L.C., 1970. Geologic Nomenclature and Classification of Porosity in
1099 Sedimentary Carbonates, AAPG Bulletin 54, 207–250. https://doi.org/10.1306/5D25C98B-16C1-
1100 11D7-8645000102C1865D
1101 Çiftçi, N.B., Temel, R.Ö., Haluk, Y.İ., 2010. Hydrocarbon occurrences in the western Anatolian
1102 (Aegean) grabens , Turkey : Is there a working petroleum system ? AAPG Bulletin 94(12), 1827–1857.
1103 https://doi.org/10.1306/06301009172
1104 Claes, H., Soete, J., Van Noten, K., El Desouky, H., Marques Erthal, M., Vanhaecke, F., Özkul, M.,
1105 Swennen, R., 2015. Sedimentology, three-dimensional geobody reconstruction and carbon dioxide
1106 origin of Pleistocene travertine deposits in the Ballık area (south-west Turkey). Sedimentology 62,
1107 1408–1445. https://doi.org/10.1111/sed.12188
1108 De Boever, E., Brasier, A.T., E., Foubert, A., Kele, S., 2017. What do we really know about early
1109 diagenesis of non-marine carbonates? Sedimentary Geology 361, 25–51.
1110 https://doi.org/10.1016/j.sedgeo.2017.09.011
1111 Deville de Periere, M., Durlet, C., Vennin, E., Lambert, L., Bourillot, R., Caline, B., Poli, E., 2011.
1112 Morphometry of micrite particles in cretaceous microporous limestones of the Middle East. Influence
1113 on reservoir properties. Marine and Petroleum Geology 28, 1727–1750.
1114 https://doi.org/10.1016/j.marpetgeo.2011.05.002
1115 Dickson, J.A.D., Saller, A.H., 1995. Identification of subaerial exposure surfaces and porosity
1116 preservation in Pennsylvanian and Lower Permian shelf limestones, eastern Central basin platform,
1117 Texas, in: Budd, D.A., Saller, A.H., Harris, P.M. (Eds.), Unconformities and porosity in carbonate strata,
1118 AAPG Memoir, 63, pp. 239-258.
1119 Dunham, R.J., 1962. Classification of Carbonate Rocks According to Depositional Textures, in: Ham,
1120 W.E. (Ed.), Classification of Carbonate Rocks, AAPG, Tulsa, pp. 108-121.
1121 Eberli, G.P., Baechle, G.T., Anselmetti, F.S., Incze, M.L., 2003. Factors controlling elastic properties
1122 in carbonate sediments and rocks. The Leading Edge 22(7), 654–660.
1123 https://doi.org/10.1190/1.1599691

1124 Ehrenberg S.N., 2007. Whole core versus plugs: Scale dependence of porosity and permeability
1125 measurements in platform carbonates. AAPG Bulletin 91(6), 835–846. 10.1306/01090706093
1126 Flügel, E., 2010. Microfacies of Carbonate Rocks. Analysis, Interpretation and Application. Berlin,
1127 Heidelberg, New York: Springer-Verlag, 984 p.
1128 Ford, T.D., Pedley, M., 1996. A review of the tufa and travertine deposits of the World. Earth-Sciences
1129 Reviews 41, 117–175. https://doi.org/10.1016/S0012-8252(96)00030-X
1130 Fortin, J., Guéguen, Y., Schubnel, A., 2007. Effects of pore collapse and grain crushing on ultrasonic
1131 velocities and Vp/Vs. Journal of Geophysical Research: Solid Earth 112(8).
1132 https://doi.org/10.1029/2005JB004005
1133 Fortin, J., Guéguen, Y., 2021. Porous and cracked rocks elasticity: Macroscopic poroelasticity and
1134 effective media theory. Mathematics and Mechanics of Solids 26(8) 1158–1172.
1135 https://doi.org/10.1177/10812865211022034
1136 Fournier, F., Borgomano, J., 2007. Geological significance of seismic reflections and imaging of the
1137 reservoir architecture in the Malampaya gas field (Philippines). AAPG Bulletin 91(2), 235–258.
1138 https://doi.org/10.1306/10160606043
1139 Fournier, F., Leonide, P., Biscarrat, K., Gallois, A., Borgomano, J., Foubert, A., 2011. Elastic properties
1140 of microporous cemented grainstones. Geophysics 76(6), E211–E226.
1141 https://doi.org/10.1190/geo2011-0047.1
1142 Fournier, F., Léonide, P., Kleipool, L., Toullec, R., Reijmer, J.J.G., Borgomano, J., Klootwijk, T., Van
1143 der Molen , J., 2014. Pore space evolution and elastic properties of platform carbonates (Urgonian
1144 limestone, Barremian-Aptian, SE France). Sedimentary Geology 308, 1–17.
1145 https://doi.org/10.1016/j.sedgeo.2014.04.008
1146 Fournier, F., Pellerin, M., Villeneuve, Q., Teillet, T., Hong, F., Poli, E., Borgomano, J., Léonide, P.,
1147 Hairabian, A., 2018. The equivalent pore aspect ratio as a tool for pore type prediction in carbonate
1148 reservoirs. AAPG Bulletin 102(7), 1343–1377. https://doi.org/10.1306/10181717058
1149 Freytet, P., 1984. Les sédiments lacustres carbonatés et leur transformations par émersion et pédogenèse.
1150 Importance de leur identification pour les reconstructions paléogéographiques. Bull. Centre Rech.
1151 Explor.-Prod. Elf-Aquitaine, Pau, 8 (1), 223-247.

Freytet, P., Verrecchia, E.P., 2002. Lacustrine and palustrine carbonate petrography : an overview. Journal of Paleolimnology 27, 221–237. https://doi.org/10.1023/A:1014263722766

García-Del-Cura, M.Á., Benavente, D., Martínez-Martínez, J., Cueto, N., 2012. Sedimentary structures and physical properties of travertine and carbonate tufa building stone. Construction and Building Materials 28, 456–467. https://doi.org/10.1016/j.conbuildmat.2011.08.042

Gassmann, F., 1951. Elasticity of porous media. Vierteljahrsschrder Naturforschenden Gesselschaft, 96, 1–23.

Harris, J.M., Nolen-Hoeksema, R.C., Langan, R.T., Van Schaack, M., Lazaratos, S.K., Rector III, J.W., 1995. High-resolution crosswell imaging of a Texas carbonate reservoir: Part I-Project summary and interpretation. Geophysics 60, 667–681. https://doi.org/10.1190/1.1443806

Heimann, A., Sass, E., 1989. Travertines in the northern Hula Valley, Israel. Sedimentology 36, 95–108. https://doi.org/10.1111/j.1365-3091.1989.tb00822.x

Herlinger, R., Zambonato, E. E., De Ros, L. F., 2017. Influence of diagenesis on the quality of Lower Cretaceous pre-salt lacustrine carbonate reservoirs from northern Campos Basin, offshore Brazil. Journal of Sedimentary Research 87, 1285–1313. https://doi.org/10.2110/jsr.2017.70

Ioakim, C., Koufos, G.D., 2009. The Late Miocene Mammal Faunas of the Mytilinii Basin, Samos Island, Greece: New Collection. 3. Palynology. Beiträge zur Paläontologie, 27–35.

Jaballah, J., Reijmer, J.J.G., Goff, J.Le, Hairabian, A., Slootman, A., 2021. Physical properties of Cretaceous to Eocene platform-to-basin carbonates from Albania. Marine and Petroleum Geology 128, 105022. https://doi.org/10.1016/j.marpetgeo.2021.105022

Jafarian, E., De Jong, K., Kleipool, L.M., Scheibner, C., Blomeier, D.P.G., Reijmer, J.J.G., 2018. Synthetic seismic model of a Permian biosiliceous carbonate – carbonate depositional system (Spitsbergen, Svalbard Archipelago), Marine and Petroleum Geology 92, 78–93. https://doi.org/10.1016/j.marpetgeo.2018.01.034

Janson, X., Eberli, G.P., Bonnaffe, F., Gaumet, F., De Casanove, V., 2007. Seismic expressions of a Miocene prograding carbonate margin, Mut Basin. AAPG Bulletin 91(5), 685–713. https://doi.org/10.1306/11020605192

1179 Jeanne, P., Guglielmi, Y., Cappa, F., 2012. Multiscale seismic signature of a small fault zone in a
1180 carbonate reservoir: Relationships between VP imaging, fault zone architecture and cohesion.
1181 Tectonophysics 554–557, 185–201. 10.1016/j.tecto.2012.05.012
1182 Jolivet, L., Faccenna, C., Huet, B., Labrousse, L., Le Pourhiet, L., Lacombe, O., Lecomte, E., Burov,
1183 E., Denèle, Y., Brun, J.P., Philippon, M., Paul, A., Salaün, G., Karabulut, H., Piromallo, C., Monié, P.,
1184 Gueydan, F., Okay, A.I., Oberhänsli, R., Pourteau, A., Augier, R., Gadenne, L., Driussi, O., 2013.
1185 Aegean tectonics: progressive strain localisation, slab tearing and trench retreat. Tectonophysics 597-
1186 598, 1–33. https://doi.org/10.1016/j.tecto.2012.06.011
1187 Kenter, J.A.M., Podladchikov, F., Reinders, M., Van der Gaast, S., Fouke, B., Sonnenfeld, M, 1997.
1188 Parameters controlling sonic velocities in a mixed carbonate-siliciclastics Permian shelf margin (upper
1189 San Andres formation, Last Chance Canyon, New Mexico). Geophysics 62, 505–520.
1190 https://doi.org/10.1190/1.1444161
1191 Kenter, J.A.M., Bracco Gartner, G.L., Schlager, W., 2001. Seismic models of a mixed carbonate
1192 siliciclastic shelf margin : Permian upper San Andres Formation, Last Chance Canyon, New Mexico.
1193 Geophysics 66(6), 1744–1748. https://doi.org/10.1190/1.1487116
1194 Kenter, J.A.M., Braaksma, H., Verwer, K., Van Lanen, X., 2007. Acoustic behavior of sedimentary
1195 rocks: Geologic properties versus Poisson's ratios. The Leading Edge 26, 436–444.
1196 https://doi.org/10.1190/1.2723206
1197 Klappa, C., 1980. Rhizoliths in terrestrial carbonates: classification, recognition, genesis and
1198 significance. Sedimentology 27, 613–629. https://doi.org/10.1111/j.1365-3091.1980.tb01651.x
1199 Kleipool, L.M., Reijmer, J.J.G., Bádenas, B., Aurell, M., 2015. Variations in petrophysical properties
1200 along a mixed siliciclastic carbonate ramp (Upper Jurassic, Ricla, NE Spain). Marine and Petroleum
1201 Geology 68, 158–177. https://doi.org/10.1016/j.marpetgeo.2015.08.017
1202 Kleipool, L.M., De Jong, K., De Vaal, E.L., Reijmer, J.J.G., 2017. Seismic characterization of switching
1203 platform geometries and dominant carbonate producers (Miocene, Las Negras, Spain). Sedimentology
1204 64, 1676–1707. https://doi.org/10.1111/sed.12369

Koufos, G.D., Kostopoulos D.S., Vlachou, T.D., Konidaris, G.E., 2011. A synopsis of the late Miocene Mammal Fauna of Samos Island, Aegean Sea, Greece. Geobios 44, 237–251. https://doi.org/10.1016/j.geobios.2010.08.004

Leiceaga, G.G., Marion, B., Sullivan, K.M.O., Bunge, G., Nielsen, J.T., Fryer, A., 2015. Crosswell seismic applications for improved reservoir understanding. The Leading Edge 34, 422–428. https://doi.org/10.1190/tle34040422.1

Lettéron, A., Fournier, F., Hamon, Y., Villier, L., Margerel , J.-P., Bouche, A., Feist, M., Joseph, P., 2017. Multi-proxy paleoenvironmental reconstruction of saline lake carbonates: Paleoclimatic and paleogeographic implications (Priarbonian-Rupelian, Issirac Basin, SE France). Sedimentary Geology 358, 97–120. https://doi.org/10.1016/j.sedgeo.2017.07.006

Matonti, C., Guglielmi, Y., Viseur, S., Bruna, P.O., Borgomano, J., Dahl, C., Marié, L., 2015. Heterogeneities and diagenetic control on the spatial distribution of carbonate rocks acoustic properties at the outcrop scale. Tectonophysics 638(1), 94–111. 10.1016/j.tecto.2014.10.020

Matonti, C., Guglielmi, Y., Viseur, S., Garambois, S., Marié, L., 2017. P-wave velocity anisotropy related to sealed fractures reactivation tracing the structural diagenesis in carbonates. Tectonophysics 705, 80–92. http://dx.doi.org/10.1016/j.tecto.2017.03.019

Matonti, C., Bourget, J., Fournier, F., Håkansson, E., Pellerin, M., Hong, F., Reijmer, J.J.G., 2021. Distinct petroacoustic signature in heterozoan and photozoan carbonates resulting from combined depositional and diagenetic processes. Marine and Petroleum Geology 128, 104974. https://doi.org/10.1016/j.marpetgeo.2021.104974

Mavko, G., Mukerji, T., Dvorkin, J., 2009. The Rock Physics Handbook: Tools for Seismic Analysis of Porous Media, Cambridge Univ. Press, Cambridge, U.K.

Meyers, W.J, 1991. Calcite cement stratigraphy : an overview, in: Barker, C.E., Kopp, O.C. (Eds.), Luminescence microscopy and spectroscopy : qualitative and quantitative applications, SEPM Short course, 25, pp. 133-148.

Mitchum, R.M., 1977. Seismic stratigraphy and global changes of sea level, Part 1: glossary of terms used in seismic stratigraphy. In Payton, C.E. (ed.), Seismic Stratigraphy—Applications to Hydrocarbon Exploration. AAPG Memoir 26, pp. 205–212.

1233 Nelson, R. A., 2001. Geologic analysis of naturally fractured reservoirs, Elsevier Science.
1234 Ordóñez, S. García-Del-Cura, M.A., 1983. Recent and Tertiary fluvial carbonates in central Spain, in:
1235 Collinson, J.D., Lewin, J. (Eds.), Ancient and Modern Fluvial System, IAS, Special Publication, 6,
1236 pp. 485–497.
1237 Parra, J. O., Hackert, C., Bennett, M., Collier, H. A., 2003. Permeability and porosity images based on
1238 NMR, sonic and seismic reflectivity : Application to a carbonate aquifer. The Leading Edge 22(11),
1239 1102–1108. https://doi.org/10.1190/1.1634914
1240 Pedley, H.M., 1990. Classification and environmental models of cool freshwater tufas. Sedimentary
1241 Geology 68, 143–154. https://doi.org/10.1016/0037-0738(90)90124-C
1242 Pedley, M., 1992. Freshwater (Phytoherm) reefs: the role of biofilms and their bearing on marine reef
1243 cementation. Sedimentary Geology 79, 255–274. https://doi.org/10.1016/0037-0738(92)90014-I
1244 Pedley, M., Hill, I., 2002. The recognition of barrage and paludal tufa systems by GPR: case studies in
1245 the geometry and correlation of hidden Quaternary freshwater carbonate facies, in: Bristow, C.S., Jol,
1246 H.M. (Eds.) Ground Penetrating Radar in Sediments, Geol. Soc. Spec. Publ., 211, pp. 207–223.
1247 Pedley, M., González MartÍn, J., Ordóñez Delgado, S., García-Del-Cura, M. Á., 2003. Sedimentology
1248 of Quaternary perched springline and paludal tufas : criteria for recognition, with examples from
1249 Guadalajara Province, Spain. Sedimentology 50, 23–44. https://doi.org/10.1046/j.1365-
1250 3091.2003.00502.x
1251 Pedley, M., 2009. Tufas and travertines of the Mediterranean region: A testing ground for freshwater
1252 carbonate concepts and developments. Sedimentology 56(1), 221–246. https://doi.org/10.1111/j.1365-
1253 3091.2008.01012.x
1254 Pe-Piper, G., Piper, D.J.W., 2007. Late Miocene igneous rocks of Samos: the role of tectonism in
1255 petrogenesis in the southeastern Aegean, in: Taymaz, T., Yimaz, Y., Dilek, Y., (Eds.), The Geodynamics
1256 of the Aegean and Anatolia, Geological Society of London, Special Publications, 291, pp. 75–97.
1257 https://doi.org/10.1144/SP291.4
1258 Purser, B.H., 1980. Sédimentation et diagenèse des carbonates néritiques récents; les éléments de la
1259 sédimentation et de la diagenèse. , Ed. Technip.

Raymer, L.L., Hunt, E.R., Gardner, J.S., 1980. An Improved Sonic Transit Time-to-Porosity Transform. In SPWLA Annual Logging Symposium, 1–13. Society of Petrophysicists and Well-Log Analysts.

Regnet, J.B., Robion, P., David, C., Fortin, J., Brigaud, B., Yven, B., 2015. Acoustic and reservoir properties of microporous carbonate rocks: Implication of micrite particle size and morphology. Journal of Geophysical Research: Solid Earth 120(2), 790–811. https://doi.org/10.1002/2014JB011313

Regnet, J.B., Fortin, J., Nicolas, A., Pellerin, M., Guéguen, Y., 2019a. Elastic properties of continental carbonates: From controlling factors to an applicable model for acoustic-velocity predictions. Geophysics 84(1), MR45–MR59. https://doi.org/10.1190/geo2017-0344.1

Regnet, J.B., David, C., Robion, P., Menéndez, B., 2019b. Microstructures and physical properties in carbonate rocks: A comprehensive review. Marine and Petroleum Geology 103, 366–376. https://doi.org/10.1016/j.marpetgeo.2019.02.022

Reijmer J.J.G., Blok C.N., El-Husseiny A., Kleipool L.M., Hogendorp Y.C.K., Alonso-Zarza A.M., 2021. Petrophysics and sediment variability in a mixed alluvial to lacustrine carbonate system (Miocene, Madrid Basin, Central Spain). Depositional Record 00, 1–23. https://doi.org/10.1002/dep2.158

Ring, U., Laws, S., Bernet, M., 1999. Structural analysis of a complex nappe sequence and late orogenic basins from the Aegean Island of Samos, Greece. Journal of Structural Geology 21(11), 1575–1601.

Salih, M., Reijmer, J.J.G., El-Husseiny, A., 2020. Diagenetic controls on the elastic velocity of the early Triassic Upper Khartam Member (Khuff Formation, central Saudi Arabia). Marine and Petroleum Geology 124, 104823. https://doi.org/10.1016/j.marpetgeo.2020.104823

Sheriff, R.E., 1977. Limitations on resolution of seismic reflections and geological detail derivable from them, in: Payton, C.E. (Ed.), Seismic stratigraphy— Applications to hydrocarbon exploration, AAPG Memoir 26, pp. 3–14.

Sheriff, R.E., Geldart, L. P., 1995. Exploration seismology, Cambridge University Press.

Soete, J., Kleipool, L. M., Claes, H., Claes, S., Hamaekers, H., Kele, S., Özul, M., Foubert, A., Reijmer, J.J.G., Swennen, R., 2015. Acoustic properties in travertines and their relation to porosity and pore types. Marine and Petroleum Geology 59, 320–335. https://doi.org/10.1016/j.marpetgeo.2014.09.004

Stafleu, J., Everts, A.J.W., Kenter, J.A.M., 1994. Seismic models of a prograding carbonate platform: Vercors, south-east France. Marine and Petroleum Geology 11(5), 514–527.

Stafleu, J., Sonnenfeld, M.D., 1994. Seismic models of a shelf-margin depositional sequence: Upper San Andreas Formation, Last Chance Canyon, New Mexico. Journal of Sedimentary Research B64(4), 481–499. https://doi.org/10.1306/D4267FEB-2B26-11D7-8648000102C1865D

Swirydczuk, K., Wilkinson, B.H., Smith, G.R., 1979. The Pliocene Glenns Ferry Oolite: lake-margin carbonate deposition in the southwestern Snake river Plain. Journal of Sedimentary Petrology 49, 995–1004. https://doi.org/10.1306/212F789C-2B24-11D7-8648000102C1865D

Teillet, T., Fournier, F., Borgomano, J., Hong, F., 2020. Origin of seismic reflections in a carbonate gas field, Lower Miocene, offshore Myanmar. Marine and Petroleum Geology 113, 104-110. https://doi.org/10.1016/j.marpetgeo.2019.104110

Thomas, H., Brigaud, B., Blaise, T., Saint-Bezar, B., Zeyen, H., Andrieu, S., Vincent, B., Chirol, H., Portier, E., Mouche, E., 2021. Contribution of drone photogrammetry to 3D outcrop modeling of facies, porosity, and permeability heterogeneities in carbonate reservoirs (Paris Basin, Middle Jurassic). Marine and Petroleum Geology 123, 104772. https://doi.org/10.1016/j.marpetgeo.2020.104772

Vail, P. R., Mitchum Jr., R. M., Thomson, S., 1977. Seismic stratigraphy and global changes of sea level, in: Payton, C.E. (Ed.), Seismic stratigraphy — Applications to hydrocarbon exploration, AAPG Memoir 26, pp. 49–212.

Vasquez, G. F., Morschbacher, M. J., Wense Dias dos Anjos, C., Moisés Parisek Silva, Y., Madrucci, V., Ramos Justen, J. C., 2019. Petroacoustics and composition of presalt rocks from Santos Basin. The Leading Edge 38, 342–348. https://doi.org/10.1190/tle38050342.1

Vincent, B., Garland, J., Gutteridge, P., Thompson, S., 2020. Unravelling the complexity of thin (sub-seismic) heterogeneous carbonate reservoirs: an integrated study of the Albian Mauddud Formation in the Greater Burgan Area, Kuwait. Journal of Petroleum Geology 43(3), 249–276. https://doi.org/10.1111/jpg.12765

Volery, C., Davaud, E., Foubert, A., Caline, B., 2010. Lacustrine microporous micrites of the Madrid Basin (Late Miocene, Spain) as analogues for shallow-marine carbonates of the Mishrif reservoir Formation (Cenomanian–early Turonian, Middle East). Facies 56(3), 385–397. https://doi.org/10.1007/s10347-009-0210-8

Weidmann, M., Solounias, N., Drake, R.E., Curtis, G.H., 1984. Neogene Stratigraphy of the Eastern Basin, Samos island, Greece. Geobios 17(4), 477–490. https://doi.org/10.1016/S0016-6995(84)80020-0

Wyllie, M.R.J., Gregory, A.R., Gardner, L.W., 1956. Elastic wave velocities in heterogeneous and porous media. Geophysics 21, 41–70. https://doi.org/10.1190/1.1438217

Xu, S., Payne, M.A., 2009. Modeling elastic properties in carbonate rocks. The Leading Edge 28(1), 66–74. https://doi.org/10.1190/1.3064148

Yu, G., Marion, B., Bryans, B., Carrillo, P., Wankui, G., Yanming, P., Fanzhong, K., 2008. Crosswell seismic imaging for deep gas reservoir characterization. Geophysics 73(6), B117–B126. https://doi.org/10.1190/1.2980417

Zeller, M., Reid, S.B., Eberli, G.P., Weger, R.J., Massaferro, J.L., 2015. Sequence architecture and heterogeneities of a field-Scale Vaca Muerta analog (Neuquén Basin, Argentina) - from outcrop to synthetic seismic. Marine and Petroleum Geology 66, 829–847. https://doi.org/10.1016/j.marpetgeo.2015.07.021

Zampetti, V.T., Sattler, U., Braaksma, H., 2005. Well log and seismic character of Liuhua 11-1 Field , South China Sea ; relationship between diagenesis and seismic reflections. Sedimentary Geology 175, 217–236. https://doi.org/10.1016/j.sedgeo.2004.12.018

Zhao, L., M.Nasser, D.Han, 2013. Quantitative geophysical pore-type characterization and its geological implication in carbonate reservoirs. Geophysical Prospecting 61(4), 827–841. https://doi.org/10.1111/1365-2478.12043

Declaration of interests

☒ The authors declare that they have no known competing financial interests or personal relationships that could have appeared to influence the work reported in this paper.

☐The authors declare the following financial interests/personal relationships which may be considered as potential competing interests: